Journal of Medicinal Chemistry

Article

Characterization of Conformationally Constrained Benzanilide Scaffolds for Potent and Selective HDAC8 Targeting

Muhammad Murtaza Hassan, Johan Israelian, Nabanita Nawar, Giovanni Ganda, Pimyupa Manaswiyoungkul, Yasir Raouf, David Armstrong, Abootaleb Sedighi, Olasunkanmi O Olaoye, Fettah Erdogan, Aaron D. Cabral, Fabrizio Angeles, Rabia Altintas, Elvin D de Araujo, and Patrick Thomas Gunning

J. Med. Chem., **Just Accepted Manuscript** • DOI: 10.1021/acs.jmedchem.0c01025 • Publication Date (Web): 16 Jul 2020

Just Accepted

is published by the American Chemical Society. 1155 Sixteenth Street N.W., Washington, DC 20036

Characterization of Conformationally Constrained Benzanilide Scaffolds for Potent and Selective HDAC8 Targeting

Muhammad Murtaza Hassan[†,‡], Johan Israelian[†,‡], Nabanita Nawar[†,‡], Giovanni Ganda[†,‡], Pimyupa Manaswiyoungkul[†,‡], Yasir S. Raouf[†,‡], David Armstrong[†], Abootaleb Sedighi[†,‡], Olasunkanmi O. Olaoye[†,‡], Fettah Erdogan[†,‡], Aaron D. Cabral[†,‡], Fabrizio Angeles[†,‡], Rabia Altintas[§,#], Elvin D. de Araujo[†], Patrick T. Gunning*[†,‡]

[†]Department of Chemical and Physical Sciences, University of Toronto Mississauga, 3359 Mississauga Road North, Mississauga, ON L5L 1C6, Canada.

[‡]Department of Chemistry, University of Toronto, 80 St. George Street, Toronto, ON M5S 3H6, Canada.

[§] Clinical Cooperation Unit Pediatric Oncology (G340), German Cancer Research Center (DKFZ), Im Neuenheimer Feld 280, Heidelberg 69120, Germany

[#]Heidelberg Medical Faculty, University of Heidelberg, Heidelberg 691171, Germany

KEYWORDS HDAC8-selective, small molecule inhibitor, conformational constraint, neuroblastoma, immunofluorescence, histone deacetylase 8 (HDAC8), benzanilide, L-shaped.

ABSTRACT: HDACs are an attractive therapeutic target for a variety of human diseases. Currently, all four FDA-approved HDAC-targeting drugs are non-selective, pan-HDAC inhibitors, exhibiting adverse side-effects at therapeutic doses. While selective HDAC-inhibition has been proposed to mitigate toxicity, the targeted catalytic domains are highly conserved. Herein, we describe a series of rationally designed, conformationally constrained, benzanilide foldamers which selectively bind the catalytic tunnel of HDAC8. The series includes benzanilides, **MMH371**, **MMH409**, and **MMH410**, which exhibit potent *in vitro* HDAC8 activity (IC_{50} = 66, 23, and 66 nM, respectively), and up to 410-fold selectivity for HDAC8 over the next targeted HDAC. Experimental and computational analysis of the benzanilide structure docked with human HDAC8 enzyme showed the adoption of a low energy L-shape conformer that favours HDAC8 selectivity. Conformationally constrained HDAC8-inhibitors present an alternative biological probe for further determining the clinical utility and safety of pharmacological knockdown of HDAC8 in diseased cells.

INTRODUCTION

Histone Deacetylases (HDACs) constitute a family of eraser proteins that are canonically known to remove acetyl groups from specific Lys side-chains of histones in order to regulate transcription. Deacetylation of Lys affords the positively charged amino group (pKa ≈ 10.3), which strengthens the electrostatic interactions between histones and the DNA backbone, reducing access to DNA by transcription factors. HDACs are known to be involved in gene transcription and other cellular processes.[1] Due to their role in gene transcription, they have the ability to increase the expression of growth promoting factors and decrease the expression of tumour suppressors.[2] Recently, HDACs have been found to have other non-histone substrates.[3–5] For instance, knockdown of over-expressed HDAC2 in colorectal cells[6] resulted in upregulation of the cyclin-dependent kinase inhibitor, p21, independent of p53, supporting the hypothesis that HDAC2 is involved in carcinogenesis.[7] Moreover, numerous studies have demonstrated increased HDAC levels in several cancers compared to normal tissues.[6,8–12]

Due to their biological roles in the progression of multiple cancers, including peripheral T-cell lymphoma (PTCL), multiple myeloma, and neuroblastoma, there is considerable interest in targeting HDACs. The United States Food and Drug Administration (FDA) has approved four pan-HDAC inhibitors to date: Vorinostat (SAHA), Romidepsin (FK228), Belinostat (PXD101) and Panobinostat (LBH-589).[10] Pan-HDAC inhibition profiles are associated with adverse side-effects such as diarrhea, thrombocytophenia, anemia and cardiac toxicity.[2,4,9,13,14] Mouse models have highlighted that selective knockdown of HDAC enzymes can improve therapeutic outcomes whereas the knockdown of other HDACs result in lethal side-effects. For instance, knockdown studies of HDAC6 and HDAC8 have resulted in impediment of tumor growth,[15,16] whereas embryonic disruption of specific HDACs (including 1, 2, 3, 7) in mouse models is associated with lethal outcomes.[11] The toxic side-effects observed in clinical trials of approved pan-HDAC inhibitors correlate with side effects observed in certain HDAC knockouts (e.g. HDAC2, 3, 5, 9).[11] Selective HDAC inhibitors (HDACi) therefore stand to have wider therapeutic windows. As a result, significant efforts towards the development of small molecule HDAC-selective inhibitors

have been made in the past decade. One of the main challenges with targeting HDACs selectively arises from the highly conserved amino acid sequence in the catalytic domain.[17–20] Although the catalytic tunnel is highly conserved, the surface topology and tunnel shape vary between HDAC family members, thus providing an opportunity for selective small molecule intervention.

HDAC8 has been implicated in multiple neurological and T-cell malignancies as well as Schistosomiasis, caused by the human flat-worm *Schistosoma mansoni*. Previous studies involving small molecule inhibition of HDAC8 have revealed unique structural features that can be exploited for selective HDAC8 ablation.[21] More specifically, soaking experiments of apo *Schistosoma mansoni* HDAC8 with HDAC8-selective inhibitors **PCI34051** (**Figure 2b**), **NCC-149**, as well as pan-HDAC inhibitor Quisinostat, indicated that HDAC8 selective inhibitors adopt an L-shape that allows them to interact with the 'HDAC8-specific pocket' formed by the catalytic tyrosine between the L1 and L6 loops (**Figure 1a**).[21] Quisinostat adopts a linear conformation that does not interact with the L1-L6 HDAC8 selectivity filter, thereby exhibiting non-selective HDAC inhibition. Furthermore, the lack of rigidity in clinically approved HDAC inhibitors (Vorinostat, Panobinstat, Belinostat etc.) afforded by their multiple rotatable centers, allows them to adapt to the various HDAC tunnel shapes, and results in pan-HDAC inhibition.

We were interested in the design of rigid L-shaped scaffolds that interact favourably with the HDAC8 selectivity pocket and are poorly accommodated by other HDACs such as HDAC6 (**Figure 1b**). The traditional pharmacophoric model of HDACi consists of three groups – the cap group, the linker, and the zinc-binding group (**Figure 2a**), with a majority of inhibitors containing flexible motifs with rotatable centers. Herein, conformationally constrained benzanilide foldamers, adopting an L-shaped conformation, are shown to afford HDAC8 tunnel selectivity (**Figure 1b, 2c**).

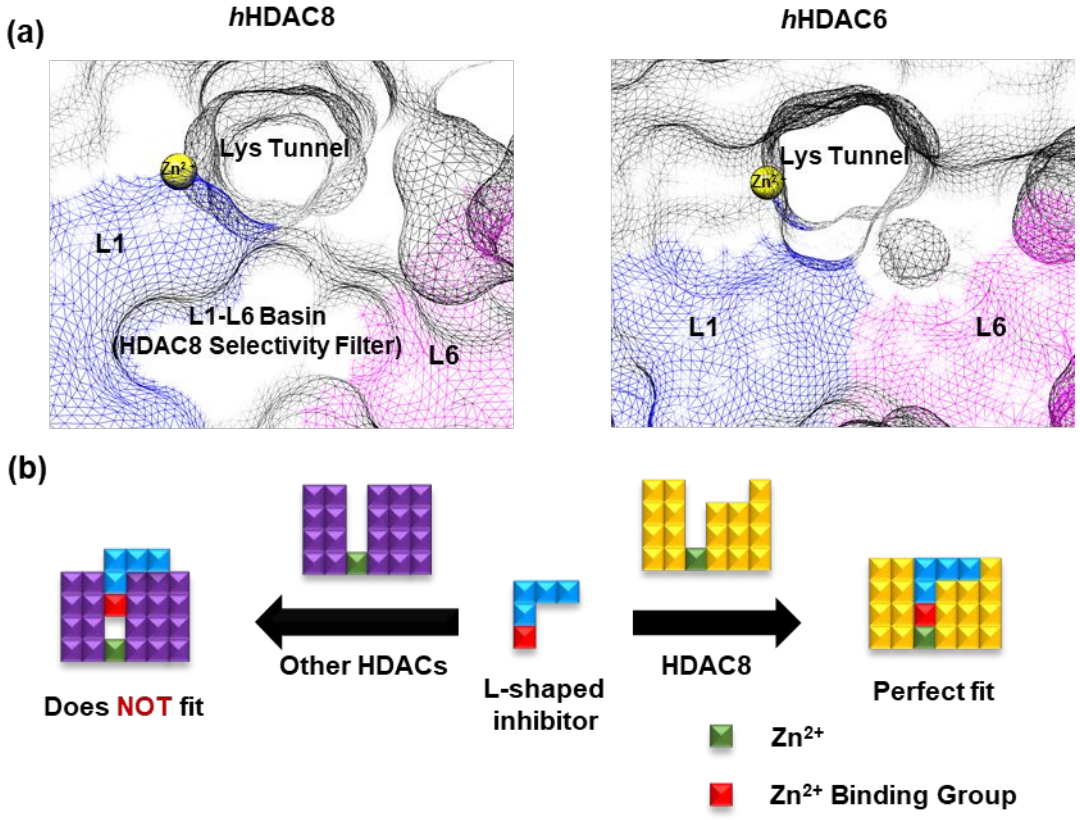

Figure 1. (a) Birds-eye view of hHDAC8 (PDB 1W22) compared to hHDAC6 (PDB 5EDU) surface topology. HDAC8 contains an L1-L6 basin whereas the L1 and L6 loops of HDAC6 are locked creating a linear Lys tunnel. (b) A 'tetris'-based model for determining HDAC8 selectivity. L-shaped inhibitors are accommodated by the HDAC8 tunnel but not in other HDACs.

RESULTS AND DISCUSSION

Structure Activity Relationship Studies. The HDAC inhibitor, 4-tert-butyl-N-[4-(hydroxycarbamoyl)phenyl]benzamide, previously published as **AES-350** (HDAC8 IC_{50} = 245 nM, HDAC6 IC_{50} = 24.4 nM)[22], was the starting point for our structure-activity relationship (SAR). Whilst more selective for HDAC6, with potency of 245 nM against HDAC8, it was hoped that a medicinal chemistry program could improve HDAC8 activity whilst reducing other HDAC potency. As part of the SAR, the potency and selectivity of each small molecule was assessed in an enzymatic-activity based Electrophoretic Mobility Shift Assay (EMSA) against HDACs 3, 6, 8 and 11 (*Nanosyn*, USA). First, moving the *t*Bu moiety on the cap-group of **AES-350** from the *para*- to *meta*- position gave **1**, and resulted in increased HDAC8 activity, while retaining HDAC6 potency

(HDAC8 IC_{50} = 34 nM, HDAC6 IC_{50} = 71 nM). To improve selectivity, it was hypothesized that *N*-amide substitution might hinder the hydroxamic acid moiety from entering the linear HDAC6 tunnel and coordinating the Zn^{2+} atom at the base of the tunnel. The hypothesis was explored first with an *N*-Et (**2**) substituent, which exhibited HDAC8 activity (IC_{50} = 83.5 nM), and >12-fold selectivity over HDACs 3, 6, and 11 (IC_{50}'s > 1 μM). Exploration of *N*-alkylated benzamides for deriving HDAC8 selective inhibitors was then conducted. Interestingly, structural studies of benzanilide-scaffolds have shown the adoption of either an *E*- or *Z* conformation (or cis and trans)-depending on the selection of substitution at *N*. For example, a proton substituent primarily favours a *Z* conformation, whereas *N*-methylated homologs favour the *E* conformation.[23] In the case of **2**, it was hypothesized that the Et group favoured an *E*-(or 'L-shaped') conformation, which was proposed to be complimentary to the topology of HDAC8's catalytic pocket (**Figure 1**).

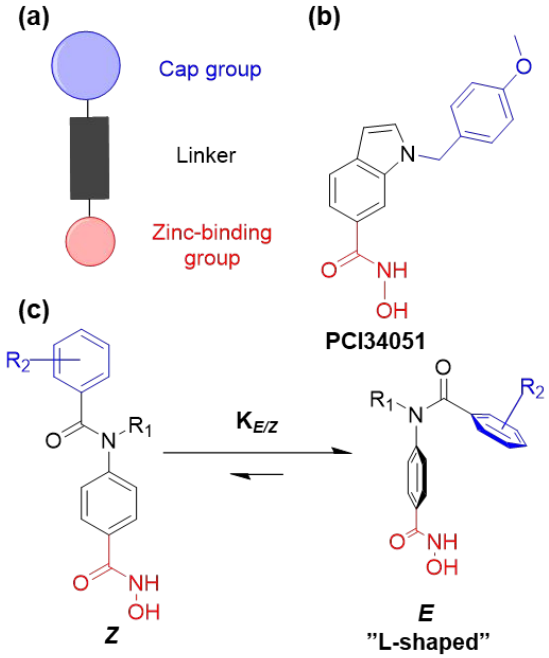

Figure 2. (a) Pharmacophoric model of HDACi. (b) Structure of PCI-34051, an HDAC8 selective inhibitor. (c) Controlling *E*–*Z* equilibrium *via* *N*-substitution of benzanilide based hydroxamic acids. *N*-H benzanilides favor the *Z* conformation whereas, *N*-alkylation (R_1 = alkyl group) favors the *E* conformation.

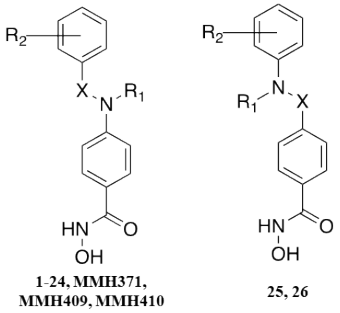

The identification of **2** prompted a thorough and systematic SAR, guided by Hirano and Marek's structural observations, to identify an HDAC8 selective pharmacophore. First, to investigate the sp^2 amide bond, compound **3**, containing a more flexible sp^3 sulfonylamide, was prepared. Compound **3** exhibited pan-HDAC activity against representative HDACs, 3, 6, and 11. This data supports the hypothesis that conformational rigidity is important for HDAC8 selectivity with benzanilide scaffolds. To better interact with hydrophobic Phe residues in the tunnel, a second *t*Bu substituent (3,5-*t*Bu) was introduced to the cap group (**7**). Despite its size, the potency and selectivity of **7** were retained, with an IC_{50} = 80 nM against HDAC8 and a > 12-fold selectivity for the nearest HDAC enzyme. Next, a 3-CF_3 substituted analog, **4**, was prepared, which marginally increased HDAC8 potency (IC_{50} = 62 nM) and selectivity (16-fold). Replacing the amide group (**4**) with a sulfonamide (**5**) resulted in a drop in potency (HDAC6; IC_{50} = 129 nM) and selectivity (>12 to 5-fold). Transposed-amide homologues, **13**, **14**, and **23**, which are unable to adopt the L-shaped conformer, showed reduced HDAC8 potency and selectivity. Additionally, an *N*-alkylated transposed amide analogue, **24**, also showed diminished HDAC8 potency and selectivity. This data supported the hypothesis that positioning of the amide, in addition to adopting the preferred L-shape, is critical to maintaining HDAC8 potency and selectivity.

Given the role of the *N*-substitution in promoting the $K_{E/Z}$ (**Figure 2c**), we probed the importance of the side group (R_1) by preparing a series of bulky *N*-aryl homologues of **4** (**8**-**10**). All benzanilides with bulky aryl side-groups, including those that incorporated the 3,5-*t*Bu benzyl (**8**) and 3-CF_3 benzyl (**9**), resulted in a loss of selectivity and potency against HDAC8. Further side-group optimization efforts included incorporation of an iPr (**16**) and methylene cPr on each of the HDAC8 selective leads, **2**, **4**, and **7**. The inclusion of iPr (**16**) had minimal effects on both potency and selectivity relative to the *N*-Et analog (**4**), whereas the inclusion of the methylene cPr group (**MMH371**, **15**, and **17**) resulted in a decrease in both potency and selectivity with the exception of **MMH371**. **MMH371**, which includes a 3-*t*Bu cap group with a methylene cPr R_1 side group, showed an increase in both potency and selectivity (HDAC8 IC_{50} = 66 nM and >15-fold selectivity). **MMH371** was also tested against the remaining class I HDAC family members in the same EMSA assay, and showed no activity against HDACs 1 and 2, IC_{50}'s >10 μM (**table S2**). Due to the potency and selectivity profiles of *N*-iPr derivatives, the *N*-iPr moiety was incorporated in a variety of subsequent derivatives. It is known that iPr and cPr groups are less-likely to be recognized and metabolized in biological systems.[24]

Table 1 –IC_{50} values for inhibitors against HDACs 3, 6, 8, and 11 in an activity-based Electrophoretic Mobility Shift Assay (EMSA) (treatment range, 0.000244 - 1 μM). Equilibrium dissociation constants (K_D) and IC_{50} independently determined using Surface Plasmon Resonance (SPR) and Fluorescence Polarization (FP) assays, respectively, against HDAC8.

Code	R_1	X	R_2	EMSA HDAC IC_{50} (μM)				SI	SPR K_D (μM)	FP IC_{50} (μM)
				3	6	8	11			
1			3-*t*Bu	>1	0.066	0.0337	>1	1.96	–	–
2			3-*t*Bu	>1	>1	0.0835	>1	>12.0	0.0261	0.203
3			3-*t*Bu	0.377	0.866	0.0553	0.802	6.82	0.0239	0.117
4			3-CF_3	>1	>1	0.0623	>1	>16.1	0.0375	0.144
5			3-CF_3	0.661	0.712	0.129	0.695	5.12	0.0459	0.340
6			3,5-CF_3	>1	>1	0.308	>1	>3.25	0.0947	0.547
7			3,5-*t*Bu	>1	>1	0.0798	>1	>12.5	0.0951	0.108
8[a]	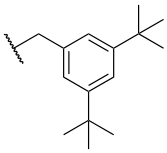		3-CF_3	>2	0.752	>2	0.673	0.337	–	3.030
9[a]	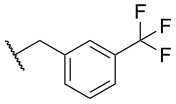		3-CF_3	>2	0.225	0.648	0.526	0.347	–	0.727
10[a]	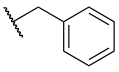		3-CF_3	>2	0.175	0.264	>2	0.663	–	0.0596
11			3-CF_3	0.254	0.0596	0.478	>1	0.124	–	0.266
12			2-CF_3	0.904	0.821	0.823	>1	0.998	–	0.368
13			3-CF_3	0.312	0.118	>1	>1	0.118	–	–
14			3,5-CF_3	>1	>1	>1	>1	0.528	–	–

15	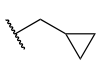		3-CF_3	>1	>1	0.116	>1	>8.62	0.00981	0.0328
16			3-CF_3	>1	>1	0.0651	>1	>15.4	0.00770	0.0625
MMH371[b]	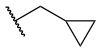		3-*t*Bu	>1	>1	0.0660	>1	>15.2	0.0108	0.0587
17	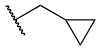		3,5-*t*Bu	>1	>1	0.225	>1	>4.44	–	Below limit
18			3,5-*t*Bu	0.0996	0.19	>1	>1	0.0996	–	–
MMH409[c]			3,5-CF_3	>1	>1	0.0234	>1	410	0.00350	0.113
MMH410[b]			3-OCF_3	>1	>1	0.0655	>1	>15.3	0.00848	0.0728
19			2-F, 3-CF_3	>1	>1	0.0885	>1	>11.3	0.00840	0.0418
20			3-CF_3, 4-F	>1	>1	0.119	>1	>8.40	0.00880	Below limit
21			3,5-*t*Bu	>1	>1	0.107	>1	>9.35	0.0260	0.0119
22			3,5-CF_3	0.672	0.112	0.682	–	0.137	–	–
23[d]			3-tBu	0.345	0.414	>1	>1	0.345	–	1.04
24[d]			3-tBu	>1	>1	0.732	>1	1.37	–	0.358
PCI34051[c]	–	–	–	>1	>1	0.00403	0.482	120	0.00310	0.134

Note: All compounds are based on the Markush structure shown on the left except for **25** and **26** and **PCI34051. PCI34051** is a known HDAC8 selective inhibitor. The Selectivity Index (SI) is calculated as a ratio between the lowest non-HDAC8 IC_{50} value and HDAC8 IC_{50} value. [a]Compounds tested at a top concentration of 2 μM. HDAC2, and 4 IC_{50} values for **8-10** were >2 μM. [b]**MMH371**, and **MMH410** were both additionally tested against HDACs 1 and 2 yielding IC_{50} values >10 μM. [c]**MMH409** and **PCI34051** were also re-tested against HDACs (1-7, 9-11) at a top concentration of 10 μM to obtain a complete selectivity profile (SI = 410). IC_{50} values for HDAC 1, 2, 4, 5, 7, 9, and 10 were >10 μM and the IC_{50} value against HDAC11 was 9.6 μM. [d]Compounds based on the Markush structure to the right. A colour gradient is applied for visualization of potency.

A 3,5-CF_3 substitution on the *N*-iPr benzanilide structure **16**, resulted in a potent and most selective HDAC8 inhibitor, **MMH409** (IC_{50} = 23 nM). A complete HDAC inhibition panel revealed a 410-fold selectivity for HDAC8 (**Table 1**, **S2**). Alternative di-substituted analogs assessed included 2-F, 3-CF_3 (**19**), 3-CF_3, 4-F (**20**), 3,5-*t*Bu (**7**), and 3-OCF_3 (**MMH410**). In addition to the 3-CF_3 substitution, fluorine substitution in the 2- and 4-positions positions (**19** and **20**, respectively) both resulted

in lower potency of 119 and 89 nM, respectively. A change in the CF_3 position from the 3-CF_3-substituted analog (**4**) to 2-CF_3 (**12**) also resulted in a loss of HDAC8 potency and selectivity. (**4**; IC_{50} = 62 nM, **12**; IC_{50} = 823 nM, **4**; SI >16, **12**; SI ~ 1). The SAR strongly supports the hypothesis that either a mono- (3-) or di-(3,5-) substituted cap-group is a favourable chemotype for improved potency and selectivity against HDAC8. Notably, previous studies have also demonstrated the use of *meta*-substituted hydroxamic acid zinc-binding groups to target HDAC8 selectively.[25–27]

Next, to confirm our hypothesis that *N*-alkylation facilitates L-shaped benzanilides and HDAC8 selectivity, we synthesized the unsubstituted *N*-amide derivatives of HDAC8 selective compounds **4**, **7**, and **MMH409**. All analogs lost HDAC8 potency (**11** (~8-fold), **18** (~13-fold) and **22** (29-fold)), and selectivity (**11** (>133-fold), **18** (>127-fold) and **22** (2994-fold)). All analogs showed increased potency against HDAC6, suggesting that *N*-H benzanilides preferentially adopt a linear conformation, more suitable for the HDAC6 tunnel.

Collectively, the benzanilide scaffold achieves HDAC8 potency and selectivity by: 1) incorporation of either a mono- (3-) or (3,5-) di-substituted (R_2) cap group; 2) a conformationally rigid amide motif (*i.e.* sp^2 carbonyl preferred rather than sp^3 sulfonyl, or methylene carbon); 3) restriction of the size of *N*-alkyl group (R_1) on the benzanilide.

***In vitro* Target Validation and Determining the Kinetic Binding Profile**. In order to corroborate the SAR trends in the EMSA activity assay, we assessed the library with an HDAC8 fluorescence polarization (FP) assay using an FP-probe, **FITC-M344** (**Table S5**).[28] HDAC8 potency in the FP assay was consistent with the trends observed in the EMSA activity assays, with **MMH371**, **MMH409** and **MMH410** all showing nanomolar IC_{50} values comparable to **PCI34051** (**PCI34051**, FP; IC_{50} = 133 nM; **MMH371**, FP; IC_{50} = 59 nM; **MMH409**, FP; IC_{50} = 110 nM; **MMH410**, FP; IC_{50} = 72 nM; **Figure 3b**, **Table 1, S5)**. In addition to the FP assessment, a Thermal Shift Assay (TSA) was performed to corroborate HDAC8-target engagement. A shift in HDAC8 melting temperature (T_m) was observed upon dosing with most HDAC8-targeting compounds (**Table S6, Figure S4, S5**). For example, **2** showed a 9 °C shift in stabilization relative to apo-HDAC8 (T_m = 37 °C) while other HDAC8 selective inhibitors only showed a 1 °C shift. HDAC8 is known to be one of the most dynamic of HDAC proteins, which may permit binding to different HDAC8 conformations and result in varying degrees of stabilization.[29,30]

The kinetic binding profile of the benzanilides was investigated using surface plasmon resonance (SPR) with full-length HDAC8 (**Figure 3c**). All of the sulfonamide derivatives showed potent equilibrium dissociation constants (K_D) of between 10 and 100 nM. *N*-alkylated benzanilides, **MMH371**, **MMH409**, **MMH410**, and **19** achieved a K_D lower than 10 nM. Notably, **MMH409** demonstrated a K_D of 3.5 nM, comparable to **PCI34051** (K_D = 3.1 nM; **Table 1**, **S3**,**S4**). The entire subset of SAR derivatives displayed similar association rate constants k_a (~10^{-5} $M^{-1}s^{-1}$, **Table S3**). The SPR results suggested that increased binding affinity was primarily due to the decrease in the kinetic dissociation rate, k_d. For instance, the *N*-Et sulfonamide, **6**, had a 30-fold lower k_d than that of the *N*-iPr-benzanilide, **MMH409**, despite both compounds containing the same 3,5-CF_3 cap-group (**Table S3, S4**). All *N*-iPr-substituted derivatives demonstrated a lower k_d when compared to their *N*-Et counterparts; **21** and **16** had a 1.8-fold and 2.4-fold lower k_d compared to counterparts **2** and **4**, respectively. The *N*-methylene cPr derivative, **MMH371** also had a marginally lower k_d (2-fold) compared to its ethylated counterpart, **2**.

Based on literature precedent, it can be assumed that the difference in *N*-alkyl group bulk (Et, iPr, and methylene cPr) is responsible for inducing a more favorable L-shape and corresponding slower dissociation rate. This also implies that the *N*-iPr and *N*-methylene cPr benzanilide scaffolds tend to have longer drug-target residence times (MRT = $1/k_{off}$) compared to their *N*-Et counterparts (**Table S3)**.[31,32] Another explanation for the decrease in dissociation rates may be due to a conformational change in the binary complex[32] after inhibitor binding, leading to a longer residence time. This is in agreement with the statistical fitting of SPR response curves using a two-state binding model[33] of *N*-iPr benzanilides **MMH409**, **MMH410**, and **21** with HDAC8 (**Table S4**, Chi^2 (RU^2) ~ 0.045-0.062).

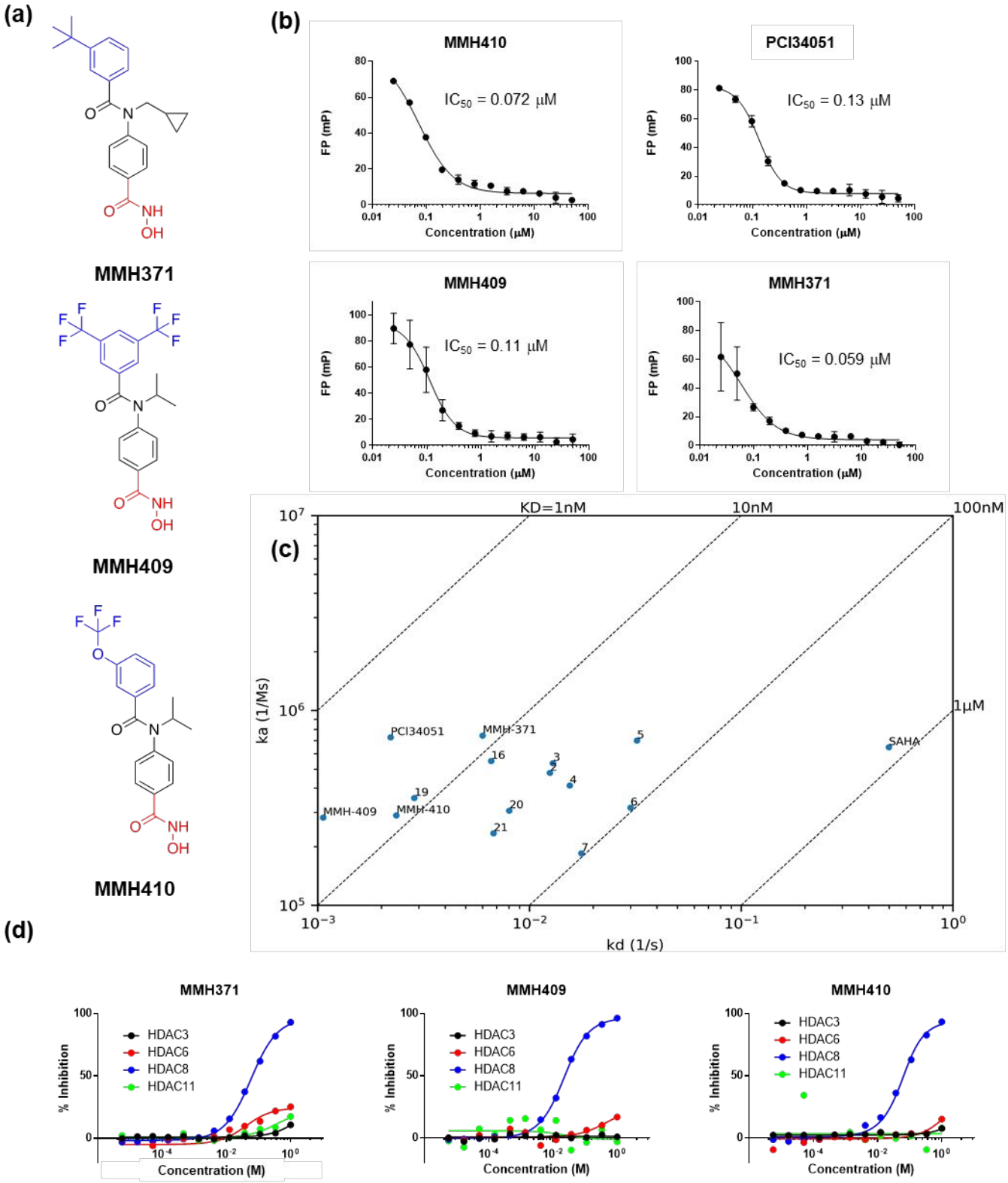

Figure 3. (a) Structures of **MMH371**, **MMH409**, and **MMH410**; (b) HDAC8 IC_{50} for **PCI34051**, **MMH371**, **MMH409**, and **MMH410** using **FITC-M344** in a competition-based Fluorescence Polarization (FP) assay[28]; (c) Logarithmic isoaffinity plot generated from rates of association (k_a) and dissociation (k_d) as determined by Surface Plasmon Resonance (SPR). The plot is divided into regions defined by their dissociation constant ($K_D = k_d/k_a$) (d) HDAC3, 6, 8, and 11 IC_{50} plots for the three compounds determined by Nanosyn using an activity-based Electrophoretic Mobility Shift Assay (EMSA).

Structural Studies of Benzanilide Scaffolds. Thus far, our hypothesis was that incorporation of small alkyl groups such as iPr (**16**, **MMH409**, **MMH410**, etc.) and methylene cPr (**15**, **17**, **MMH371**) impart HDAC8 selectivity via an *E* conformation (**Figure 1b, 2c**). X-ray crystal structures of **MMH371** and **MMH409**, confirmed that both molecules had non-linear conformations in the crystallized state (**Figure 4b**). The structures revealed the close proximity of the aryl groups of the cap- and linker moiety for both **MMH371** and **MMH409**, with the distance between the *ortho*-hydrogens of the cap-group and linker, being 3.105 Å and 2.995 Å, respectively. The two phenyl motifs of the benzanilide scaffold were approximately perpendicular to each other. In **MMH371**, the distance between the *ortho*-protons of one phenyl ring to the other (3.206 Å) was larger than in **MMH409**, with the bulky *t*Bu group oriented away from the hydroxamic acid substituted phenyl ring. 2D-NOESY experiments of *N*-alkylated HDAC8-selective inhibitors, **16**, **17**, **20** and **MMH409** all showed ^{1}H-^{1}H NOE correlations between the protons from the two phenyl rings (**Figure 4c, S10**) confirming the *E* conformation is retained in solution (deuterated methanol). For instance, **17** (**Figure 4c**) showed a strong NOE correlation consistent with the L-shaped configuration. As expected, the *N*-H benzanilides, **11**, **18** and **22**, showed no NOE correlations in solution (**Figure S11**). DFT analysis was performed on the HDAC8 library to correlate the dependence of HDAC8-selectivity on L-shaped conformation. The *E-Z* equilibrium constant $K_{E/Z}$ (**Figure 2c, 4a**) was predicted for the complete SAR using Gaussian at the ωB97XD/6-31++G(d,p) level of theory with Polarizable Continuum Model (PCM) water solvent correction by determining the Gibbs free energy of the *E* (G_E) and *Z* (G_Z) foldamers (**Table S11**). The *E-Z* equilibrium constant ($K_{E/Z}$) was calculated by using $\Delta G_{E/Z}$ (**Equation 1**).

$$G_E - G_Z = -RTln(K_{E/Z}) \quad \textbf{(1)}$$

A plot of log $K_{E/Z}$ versus the selectivity of HDAC8 molecules (**Figure 5d**) was used to computationally determine the dependence of HDAC8 selectivity on the conformational bias of the HDAC8 SAR library. A log $K_{E/Z} > 1$ represents an *E* conformer population of > 90%. Interestingly, all of the HDAC8 selective molecules with an SI > 8 displayed a log $K_{E/Z} > 1$ indicating a high-preference for the *E* (L-shaped) conformation. The *N*-H benzanilides **(1, 11, 22**) had >90% *Z* population with the exception of **20**, a 3,5-*t*Bu cap group benzanilide (~72% *Z*, **Table S11**).

Although, some of the sulfonamides (**3, 5**) displayed some selectivity due to their flexible sp^3 sulfur atom, their *E-Z* equilibrium was much lower, while still predominantly preferring the *E* conformation (% *E* = 56 and 70 %, respectively). Some *N*-aryl benzanilides however (**9, 10**), do not display HDAC8 potency despite their preference for the *E* conformation as predicted by DFT (~96% and ~95% *E,* respectively, **Table S11**). We presume that the greater steric bulk of **9** and **10** may prevent entry into the HDAC8 tunnel, thereby reducing its activity. Similarly, one of the *N*-alkylated transposed amides, **24**, although preferring the L-shape (log $K_{E/Z}$= 1.74, % *E* = 98%), is not potent against HDAC8 (IC_{50} = 732 nM). It is hypothesized that transposition of the amide may result in a steric clash between the *N*-alkyl group and the tunnel entrance residues, or, result in a loss of favourable H-bonding interactions with the tunnel entrance residues. X-ray and NMR studies of our benzanilide-based hydroxamic acid pharmacophores confirmed previous conformational studies conducted on the effect of *N*-alkylation on conformation.[23,34–39] While HDAC8 selectivity is proposed to be due to the adoption of the L-shape, there are additional factors, such as sterics and intermolecular bonding, that can also contribute to HDAC8 selectivity, or lack thereof.

***In Silico* Docking Studies.** In order to validate the mode of binding of HDAC8 selective inhibitors, *in silico* computational studies were performed using Schrödinger Maestro 11.9.011 software with Glide within the Small-Molecule Drug Discovery Suite 2019-1.[40–42] The HDAC8 inhibitor library was docked with hHDAC8 (PDB: 1W22) and docking scores were reported as a free energy of binding (ΔG_B) in the supplementary section (**Table S12**). All of the *N*-H benzanilides (**1, 18**, and **22**), with the exception of **11**, showed a higher ΔG_B than their *N*-iPr and N-methylene cPr HDAC8 selective counterparts, in agreement with the activity assays. Compound **1** had a ΔG_B of -8.097 kcal/mol as compared to its *N*-methylene cPr HDAC8-selective analogue, **MMH371**, which was calculated to have an ΔG_B of -8.563 kcal/mol. Similarly, **18** and **22**, had docking scores of -4.680 kcal/mol and -4.696 kcal/mol, whereas their *N*-iPr HDAC8 selective counterparts, **21** and **MMH409** had a ΔG_B of -4.725 kcal/mol and -7.873 kcal/mol, respectively. The three HDAC8 selective leads **MMH371**, **MMH409** and **MMH410** were chosen for studying the docking poses in comparison with the *N*-H benzanilides **1**, **11**, **18**, and **22**. All three inhibitors showed binding to hHDAC8 in their L-shaped conformation, with the cap-groups bound in the HDAC8 L1-L6 basin (**Figure 5**). This was consistent with previous HDAC8-inhibitor structural studies that indicated that HDAC8-selective inhibitors bind to a unique HDAC8-selective pocket formed by a catalytic tyrosine and L1-L6 loops.[21] The *N*-H benzanilides were accommodated within the lysine tunnel in a linear fashion as predicted by DFT analysis without any interaction with the L1-L6 basin.

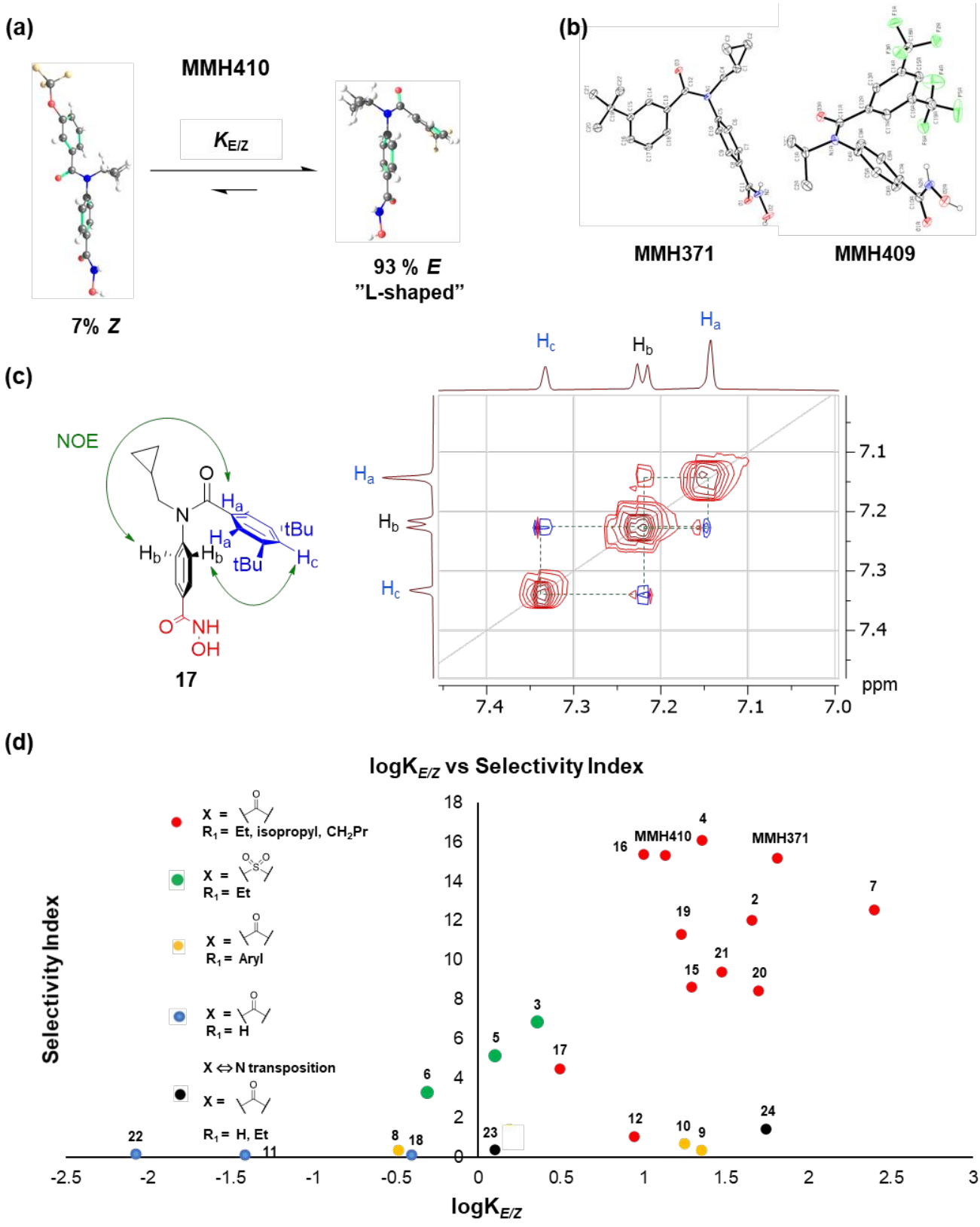

Figure 4. *N*-alkylation of benzanilide scaffolds facilitate adoption of an *E* or L-shaped conformation. (a) The *E-Z* equilibrium of the benzanilide **MMH410**. **MMH410** is 93% *E* as predicted by DFT analysis. The *E-Z* equilibrium of **MMH410** depends on R_1 composition; (b) X-ray crystal structures of **MMH371** and **MMH409**; (c) Two-dimensional NOESY experiment on **17**, a potent and selective HDAC8 inhibitor, showing NOE

correlations consistent with the L-shape; (d) A log $K_{E/Z}$ versus HDAC8 selectivity plot, showing the dependence of HDAC8 selectivity on the *E-Z* benzanilide equilibrium. ΔG of *E-Z* equilibrium was calculated using Density Functional Theory (DFT) analysis of the HDAC8 SAR and used to determine Log $K_{E/Z}$. All values for Selectivity Index (SI), were plotted as the maximum reported value and are likely underestimates of the true HDAC8 selectivity. For example, **17** displayed SI >4.44, and the value 4.44 was used for the plot.

Determining Biological Applicability. Lead compounds, **MMH371**, **MMH409**, and **MMH410**, were evaluated for cellular permeability by conducting a Parallel Artificial Membrane Permeability Assay (PAMPA) (**Table 2**).[43] In the PAMPA assay, methotrexate and testosterone were used as negative and positive controls, respectively. A permeability coefficient ($-\text{Log } P_e$) lower than 6 generally defines a compound as having a high permeability profile. All compounds tested displayed a $-\text{Log } P_e < 6$ predicting a high permeability profile (**Table 2, S7**). To gauge structural stability, compounds were assessed for stability in human plasma. **MMH371** and **MMH-410** demonstrated good stability in human plasma ($t_{1/2} > 4$ h) with **MMH409** being less stable (~1.5 h, **Table 2**).

Table 2 – Properties of top three HDAC8 selective molecules. *In vitro* permeability (-Log P_e and % recovery) and stability profiles ($t_{1/2}$) in human plasma.

Compound ID	PAMPA		*Plasma Half-life* $t_{1/2}$ (min)[a]
	-Log P_e	Recovery%	
MMH371	5.70	102.5	278
MMH409	5.42	95.4	93
MMH410	5.80	101.8	266

[a]Half-life determined from an average of three runs.

While not fully understood, the disease relevance of aberrant HDAC8 activity has been implicated in advanced-stage neuroblastoma.[3,9,44] Neuroblastoma is a childhood extracranial solid-tumour associated with a lack of differentiation and maturation of neural crest cells, and <50% long-term survival probability of high-risk patients.[3] Additionally, patients that undergo chemotherapy suffer from immediate and long-term toxicities, which makes newer therapies with minimal toxicities, such as those targeting cell maturation, highly desirable.[3,45] The three lead HDAC8 inhibitors were assessed in a neuroblastoma cell (BE(2)-C colony assay and the potency was determined. It was found that **MMH371** (IC_{50} = 2.1 μM) was essentially equipotent with known HDAC8 inhibitor, **PCI34051** (IC_{50} = 3.1 μM) (**Figure 6a**).

Immunofluorescence imaging in neuroblastoma cells (BE(2)-C) was employed to determine the acetylation levels of the HDAC8 substrate, Structural Maintenance of Chromosomes protein 3 (SMC3), after being dosed with **MMH410**.[3,26,44,46,47] Inhibition of HDAC enzymes typically leads to increased acetylation of their substrates. Immunofluorescence imaging revealed a dose-dependent increase in acetylation levels similar to that of **PCI34051** (**Figure 6c, S15**). The neuroblastoma cells were found to form visible clusters upon addition of **MMH410**, which may be indicative of a stress response.[48] Furthermore, Western blot analysis of Ac-SMC3 and Ac-tubulin (HDAC6 substrate) demonstrated *in cellulo* HDAC8 selectivity over HDAC6 for **MMH410** whereas **MMH371** did not. Ac-SMC3 showed a dose-dependent increase for **MMH371** and **MMH410**, whereas Ac-tubulin remained constant even at a concentration of 10 μM for **MMH410** but showed a dose-dependent increase for **MMH371** (**Figure 6d**). **MMH410** displayed a greater selectivity for HDAC8 in cells than **MMH371**.

MMH371 and **MMH410** were selected for further stability profiling to determine their application as *in vivo* probes. CD-1 mice were given HDAC8 inhibitors interperitoneally (IP), at a single dose (100 mg/kg), and blood was collected at multiple time points over a 12 h period post-administration. **MMH371** exhibited a modest increase in $t_{1/2}$ as compared to **PCI34051** (4.1 h vs. 3.3 h, respectively; **Figure 6b**). While the maximal concentration, C_{max}, (2893 ng/mL, 7.88 μM) was significantly lower than that of **PCI34051** (C_{max} = 16967 ng/mL, 57.6 μM), their overall exposures were comparable (**MMH371**, AUC_{last} = 5851 h*ng/mL; **PCI34051**, AUC_{last} = 6946 h*ng/mL; **Table S9, S10**). **MMH410** was shown to exhibit a $t_{1/2}$ comparable to **PCI34051**, but exhibited a significantly lower maximal concentration and exposure ($t_{1/2}$ = 2.7 h; C_{max} = 440 ng/mL, 1.14 μM; AUC_{last} = 1653 h*ng/mL; **Figure 6b**, **table S8**). **MMH371** and **MMH410** both demonstrated a greater *in vivo* mean residence time (MRT) over **PCI34051** (**MMH371**, MRT = 2.77 h; **MMH410**, MRT = 3.00 h; **PCI23051**, MRT = 0.45 h; **Table S8**, **S9**, **S10**).

Conclusion and Future Remarks. HDAC selective inhibitors are hypothesized to prevent or lower acute therapy related toxicities associated with pan-HDAC inhibitors. One approach to achieving selectivity has been to exploit the topological differences between various HDACs.

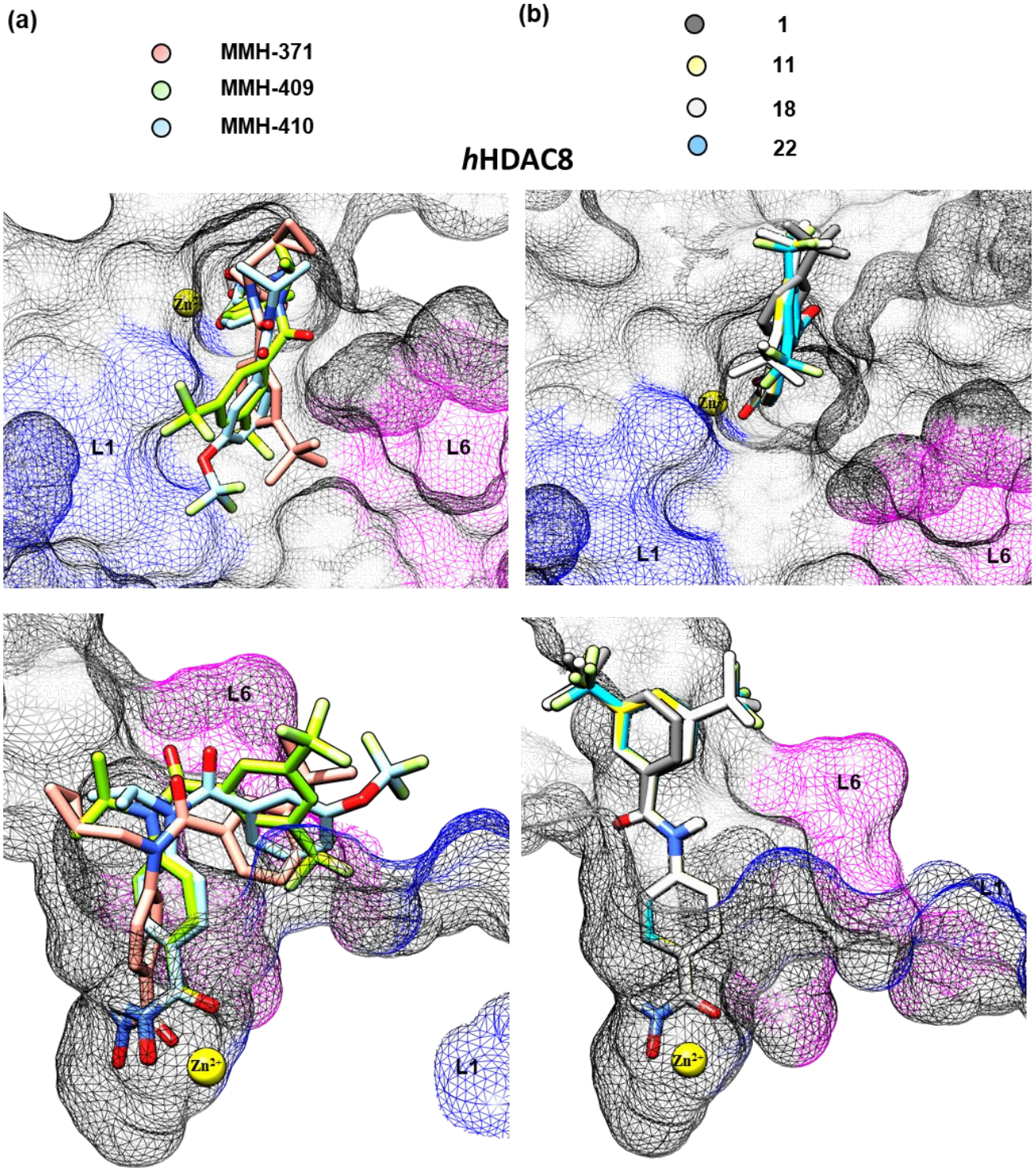

Figure 5. Computational docking studies to determine mode of action of *N*-alkylated versus *N*-H benzanilide scaffolds against hHDAC8 (PDB 1W22). (a) Three HDAC8 selective inhibitors (**MMH371**, **MMH409**, and **MMH410**) overlaid and docked onto hHDAC8. The *N*-alkylated benzanilide scaffolds adopt an L-shape where the cap-groups dock in the L1-L6 basin. (b) The *N*-H benzanilide scaffolds (**1**, **11**, **18**, **22**) preferentially adopt a linear conformation that is unable to interact with the L1-L6 basin.

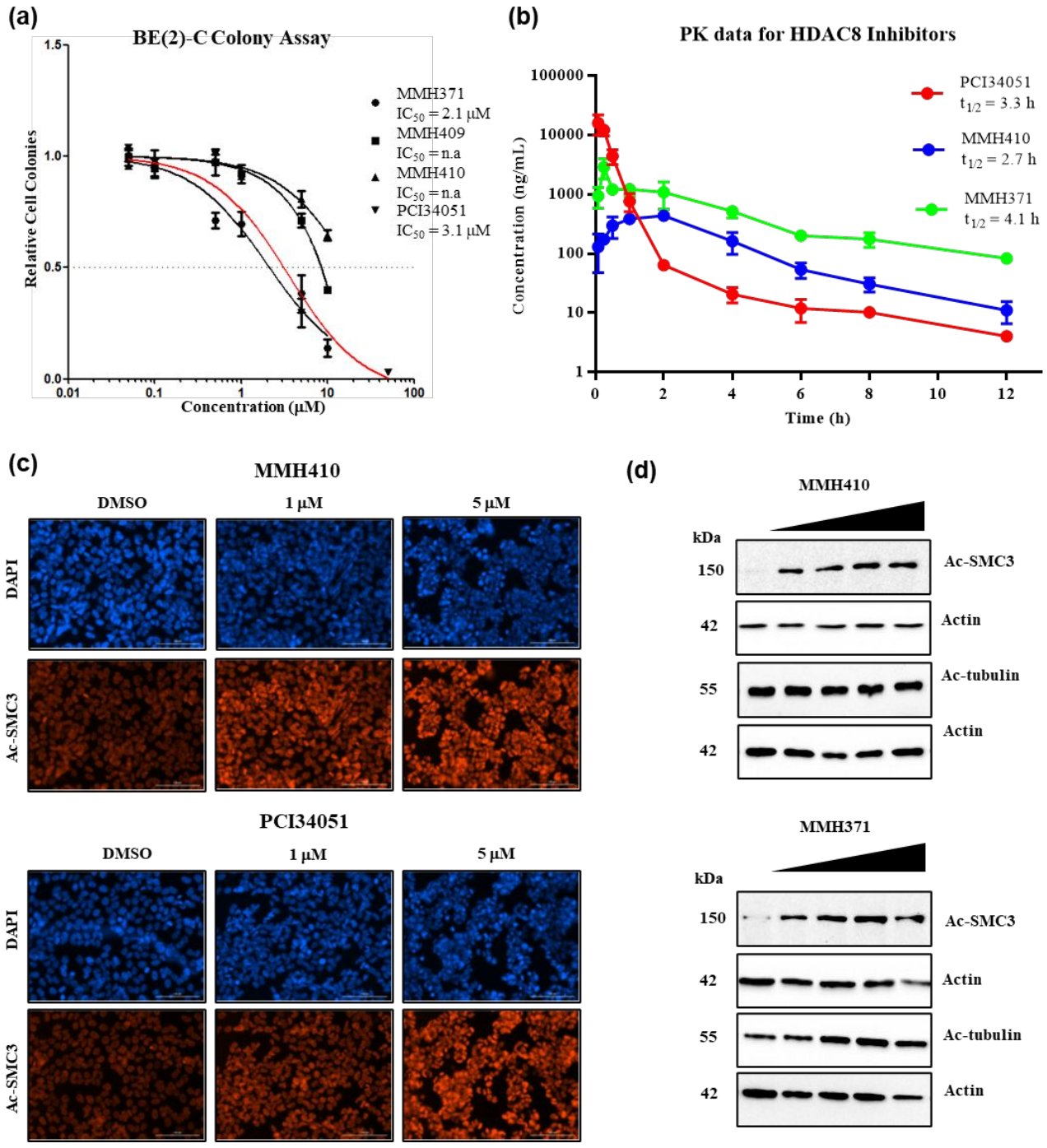

Figure 6. (a) Colony assay of neuroblastoma (BE(2)-C) cells with three HDAC8 selective inhibitors (**MMH371**, **MMH409**, **MMH410**). (b) *In vivo* half-life of **MMH371** ($t_{1/2}$ = 4.1 h), **MMH410** ($t_{1/2}$ = 2.7 h) and **PCI34051** ($t_{1/2}$ = 3.3 h) in CD-1 mice dosed at 100 mg/kg, measured as a function of time (h) versus concentration (ng/mL) of MMH410 in blood. (c) Immunofluorescence images of DAPI (blue) nuclear staining and Ac-SMC3 (red) showing a dose dependent increase of Ac-SMC3 upon addition of MMH410 and PCI34051. (d) Western blot analyses of Ac-SMC3 and Ac-tubulin in BE(2)-C cells treated with **MMH410** and **MMH371** (DMSO, 2.5, 5, 7.5, and 10 μM).

In this study, we have developed a series of potent and selective HDAC8 inhibitors based on the conformational restrictions afforded by *N*-alkylated benzanilides. We have shown the following: (1) A thorough SAR demonstrating the structural determinants required for HDAC8 selectivity; (2) *N*-alkylation of benzanilides affords an L-shaped conformation required for HDAC8 selectivity; (3) the biological utility of L-shaped benzanilides as potential chemotherapeutics and biological probes. The current FDA approved HDAC inhibitors have pan-inhibition profiles due to their predominantly linear conformation and/or conformational degrees of freedom which permit interaction with a variety of HDAC catalytic Lys tunnels. Utilizing conformationally rigid scaffolds for exploiting tunnel shapes and specific surface topologies is a promising strategy for

attaining HDAC protein-selectivity. The conformationally constrained benzanilide foldamer-based hydroxamic acid pharmacophore presents an interesting pharmacophore for achieving selective targeting of HDAC8.

EXPERIMENTAL DETAILS

General Methods. All solvents and chemicals were purchased from Sigma-Aldrich, Combi-Blocks, Alfa-Aesar, Caledon Laboratory Chemicals, and Oakwood Chemical. Anhydrous solvents such as methanol, acetonitrile, and DMF were used from anhydrous-grade Sure-Seal bottles without further drying treatments. THF, DCM, DCE, and chloroform were dispensed using the MBraun-Solvent Dispensary System (MB-SPS). All reactions under non-aqueous conditions were conducted in oven-dried glassware. Reaction progress was monitored by Thin Layer Chromatography (TLC) and visualized by Ultraviolet light (UV, 254/365 nm). Microwave irradiation was carried out in an Initiator Sixty Biotage apparatus at a high-absorption setting at 2.54 GHz.

A 400 MHz Bruker, 600 MHz Agilent DD2, and 700 MHz Agilent DD2 NMR spectrometer equipped with an HCN cryoprobe, were used to collect ^{1}H, ^{13}C, and ^{19}F NMR spectra. Two dimensional ^{1}H-^{1}H Nuclear Overhauser Spectroscopy (NOESY) studies were conducted on the 700 MHz Varian at room temperature in deuterated methanol. All deuterated solvents for NMR were purchased from either Sigma-Aldrich or Cambridge Isotope Laboratories. Chemical shifts (δ) are reported in parts per million after calibration to the residual solvent peak from the deuterated solvent. Coupling constants (*J*) are reported in Hertz (Hz) and multiplicities are reported as follows: singlet (s), doublet (d), triplet (t), quartet (q), pentet (p), sextet (sex), septet (sep), multiplet (m), broad (br), and the combination of these is represented as a combination of their abbreviations (eg. doublet of triplet (dt)). Low-resolution mass spectrometry (LRMS) using Waters LC-MS equipped with a Micromass ZQ MS in both positive and negative ESI modes was used to confirm the success of the reaction along with NMR. High-resolution mass spectrometry was performed for all final compounds at the Advanced Instrumentation for Molecular Structure (AIMS) at the University of Toronto using the Agilent 6538 Ultra High Definition (UHD) Accurate-Mass Q-TOF LC/MS System.

Column Chromatography was conducted using a gradient of ethyl acetate and hexane on manually packed SNAP 10, 25, 50, 100 g cartridges with 40-60 μm silica gel on a Biotage system. Compounds were wet-loaded by dissolving in minimal DCM or dry-loaded by adsorbing onto silica gel. Flow rates 12, 25, and 50 mL/min were used for cartridges SNAP 10, 25, 50 and 100 respectively. Compounds were detected by measuring absorbance at 254 nm and 280 nm. Preparatory High-Performance Liquid Chromatography (PrepHPLC) was carried out on all final compounds to ensure a final purity >95%. The PrepHPLC was equipped with an XSelect CSH Phenyl-Hexyl C18 column (30 x 250mm), a Waters 2489 Dual Absorbance UV-Visible Detector, a Waters 2545 Quaternary Gradient Module, and a Waters 2707 Autosampler. All compounds were detected using 254/280 nm UV-light and purified using a linear gradient of a mixture of H_2O and 0.1 % formic acid (A), and acetonitrile and 0.1% formic acid (B) using two different methods as indicated. The methods are illustrated below as the linear gradient of B depicted by its % (v/v) composition and its time duration at a flow rate of 50 mL/min.

Method 1: 2% → 100% over 50 minutes then 100% for 10 minutes

Method 2: 5% → 100% over 50 minutes then 100% for 10 minutes

Analytical HPLC was used to determine the purity of final compounds after PrepHPLC. It was carried out using a Phenomenex Luna 5.0 μm C18 4.6 mm x 150 mm column fitted on a Hewlett Packard Series 1100 analytical HPLC at a flow rate of 1.2 mL/min using method 1 and 2 as indicated. Compound purity is reported as the relative area of the compound peak to all other peaks on the chromatogram. The retention time (t_R) for each peak is reported in minutes. The purity of all compounds reported is >95% as determined by the analytical HPLC.

X-ray diffraction data were collected on a Bruker Kappa APEX-DUO diffractometer using a Copper ImuS (microsource) tube with multi-layer optics and were measured using a combination of f scans and w scans. The data were processed using APEX3 3 (Bruker, 2018). Absorption corrections were carried out using SADABS.[49] The structures were solved using SHELXT[50] and refined using SHELXL-2018[51] for full-matrix least-squares refinement that was based on F^2.

Synthesis of 2-9, 11 (skipped STAB step), 12, 15-17, 19-21, MMH371, MMH409, and MMH410

Scheme 1

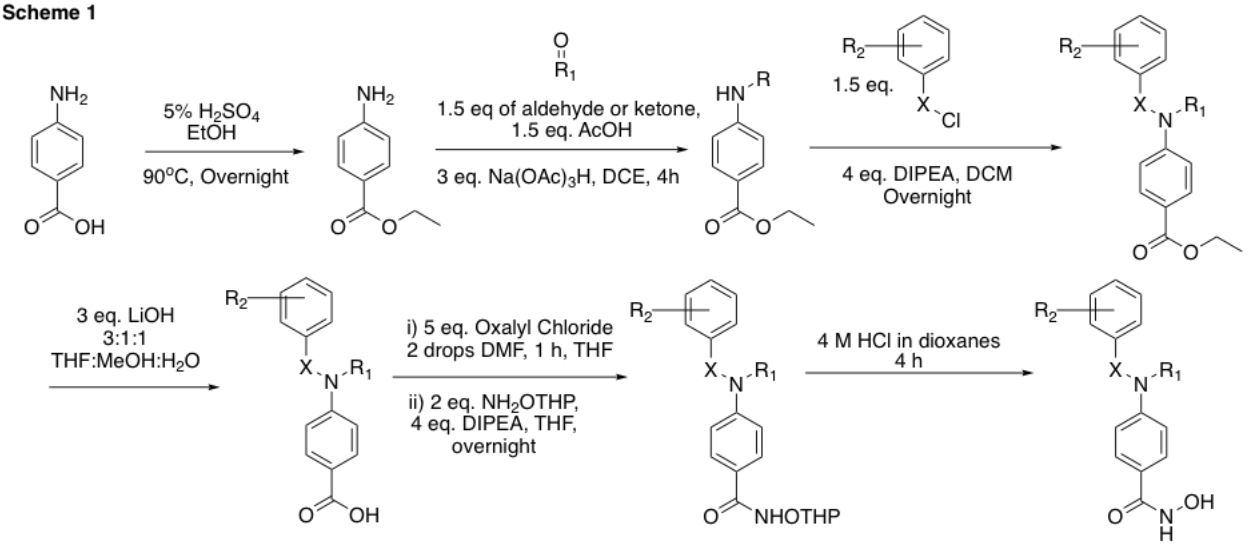

Synthesis of 10

Scheme 3

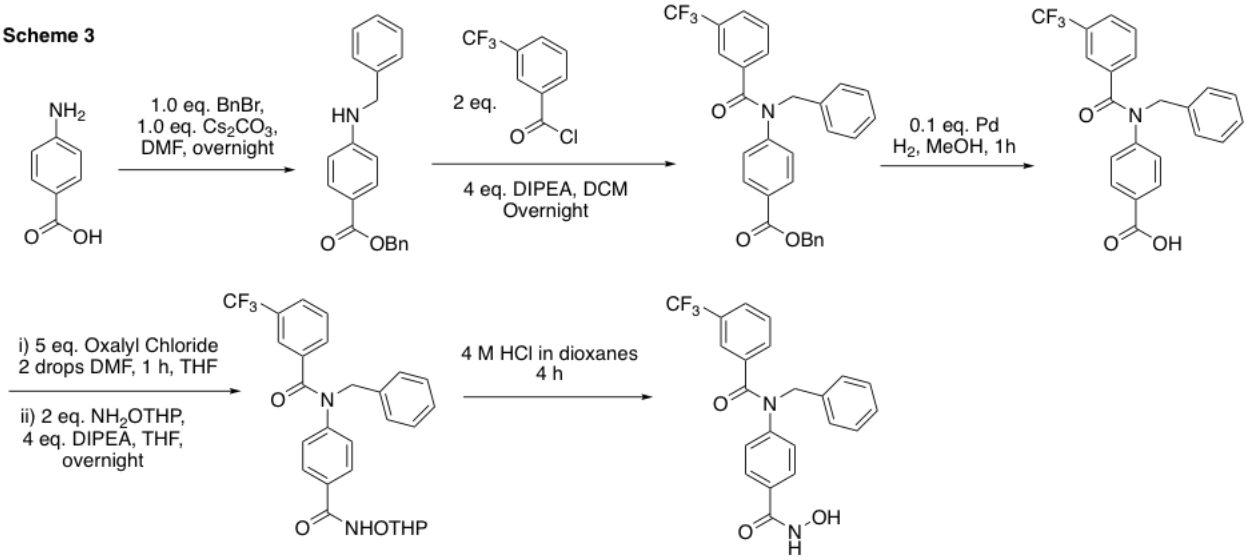

Synthesis of 13, and 14

Scheme 4

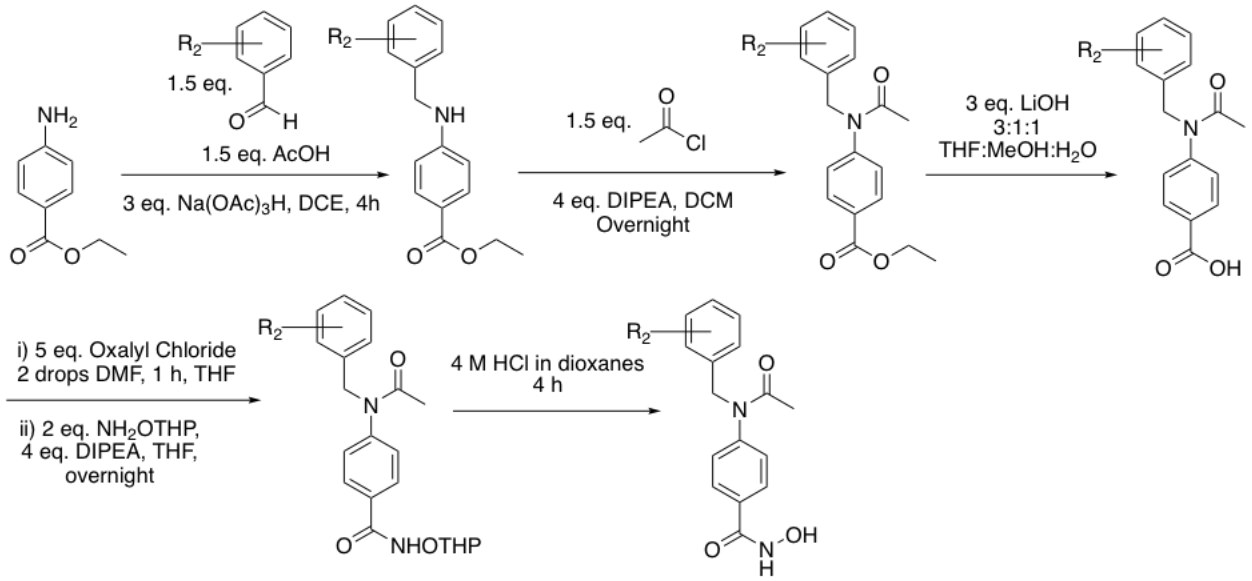

Synthesis of 23 and 24

Scheme 5

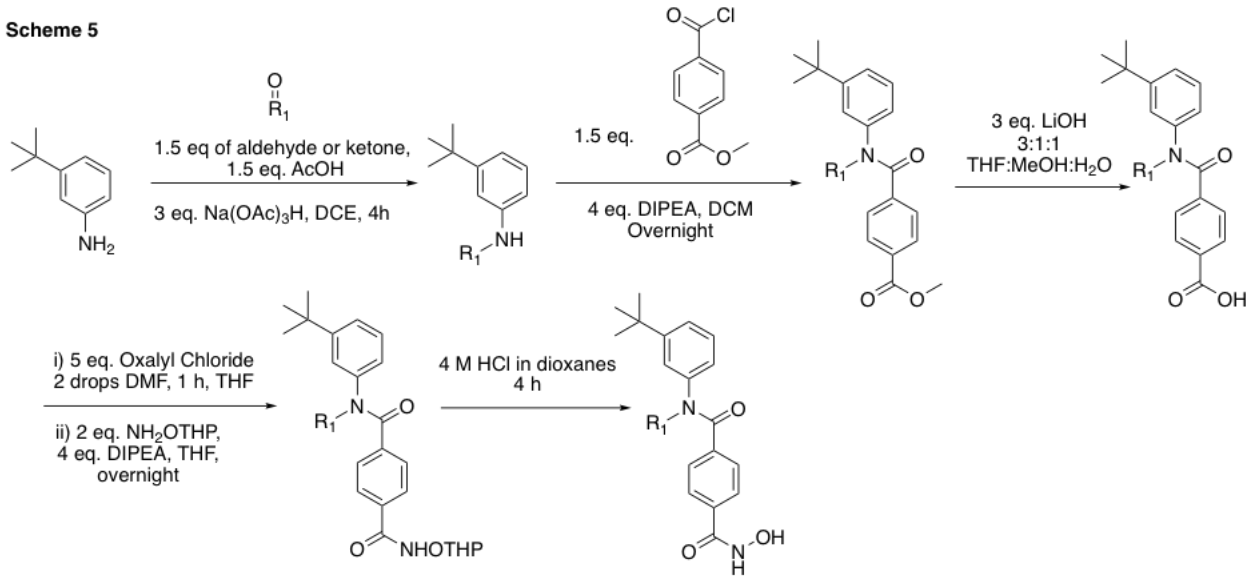

Note: First step was skipped for **23**.

Esterification of 4-aminobenzoic acid

To a solution of 0.1 mmol/mL solution of 4-aminobenzoic acid in ethanol was added sulfuric acid to make a sulfuric acid:ethanol ratio of 1:20. The reaction was heated to 90 °C overnight then diluted with ethyl acetate and extracted with 0.5 M NaOH followed by a brine wash. The solution was concentrated *in vacuo* to give a peachy-flaky solid.

Reductive amination of aryl amines

Aryl amines from schemes 1,4 and 5 were dissolved in DCE to make a 0.1 mmol/mL solution. Subsequently, the respective aldehyde (1.5 eq.), acetic acid (1.5 eq.), sodium triacetoxyborohydride (STAB, 3 eq.) and one scoop of $MgSO_4$ were added concurrently. The reaction was stirred for 4 hours and concentrated *in vacuo* and adsorbed onto silica gel. The crude mixture with silica was dry-loaded for column chromatography which afforded the desired intermediates.

Acylation/sulfonylation of aryl amines

To a solution of the respective sulfonyl or acyl chloride (1.5 to 2 eq.) in dichloromethane (0.1 mmol of aryl amine/mL) was added diisopropyl amine (DIPEA, 4 eq.) which produced a smoke suspended above the solution. Then aryl amine was added, and the solution was left to stir overnight. The solution was dried *in vacuo* with silica gel for dry-loading on a column for column chromatography which yielded the desired intermediates.

Deprotection of methyl/ethyl esters

To a solution of THF, methanol and MilliQ H_2O in a ratio of 3:1:1 containing the methyl/ethyl ester (0.1 mmol/mL) was added lithium hydroxide (3 eq.). The mixture was left to stir overnight. The reaction was complete in approximately 16 hours as indicated by TLC and LRMS. The solution was diluted with ethyl acetate and washed twice with 1 M HCl followed by a brine wash and drying with magnesium sulfate. Drying *in vacuo* yielded relative pure intermediates that were used directly for the subsequent step without further purification.

Synthesis of THP-protected hydroxamic acids

The aryl carboxylic acid intermediates were converted to their acyl chloride intermediates by the use of the Vilsmeier-Haack reagent generated *in situ*. The aryl carboxylic acid intermediate was added to a solution of THF (0.1 mmol/mL), followed by the addition of no more than two drops of DMF, and oxalyl chloride (5 eq.) which caused immediate effervescence. The solution was purged with nitrogen gas until the effervescence halted. The reaction was then stirred for 1 hour under inert atmosphere. The solution containing the acyl chloride was dried immediately *in vacuo* (15 min rotary evaporator followed by 15 min high-vacuum) with minimal exposure to air and moisture. The crude mixture was re-dissolved in THF, and DIPEA (4 eq.) was added, resulting in a layer of smoke above the solution. Subsequently, *O*-(Tetrahydro-2*H*-pyran-2-yl)hydroxylamine (2 eq.) was added and the mixture was left to stir overnight. Drying *in vacuo* followed by column chromatography yielded the desired THP-protected hydroxamic acid.

Deprotection of the THP-protected hydroxamic acids

The THP-protected hydroxamic acid was dissolved in 4 M hydrochloric acid in dioxanes (0.1 mmol/mL dioxane) and left to stir for 4 hours. The reaction was monitored by TLC and LRMS which indicated a complete conversion. The solution was dried *in vacuo* and the crude mixture was purified by Preparative HPLC.

Benzyl protection of 4-aminobenzoic acid

4-aminobenzoic acid was dissolved in DMF (2 mmol/mL) and stirred with Cs_2CO_3 (1.1 eq.) for 20 minutes. Benzyl bromide (1 eq.) was added subsequently, and the solution was stirred overnight. The mixture was diluted with ethyl acetate and washed thrice with water followed by a brine wash. Drying by $MgSO_4$ and concentrating *in vacuo,* followed by column chromatography afforded two products: a peachy mono-O-benzylated product, and another di-N,O-benzylated product (used for scheme 3).

Benzyl deprotection of benzyl ester intermediates

To a solution of benzyl ester in THF (0.1mmol/mL) was added methanol to make a THF:methanol ratio of 2:1. The solution was purged with nitrogen for 15 minutes before the addition of 10% palladium on carbon (0.1 eq.) followed by another 5 minute nitrogen purge. Hydrogen gas was bubbled through the solution for 1 hour using a long-needle submerged in the solution. TLC indicated the reaction was complete and the reaction was diluted with ethyl acetate and filtered through celite.

3-(*tert*-butyl)-*N*-(4-(hydroxycarbamoyl)phenyl)benzamide (1). ^{1}H NMR (400 MHz, DMSO-d_6) δ 10.77 – 10.71 (br, 1H), 8.70 – 8.61 (m, 1H), 7.51 – 7.19 (m, 6H), 6.65 (d, J = 8.4 Hz, 2H), 1.19 (s, 9H). ^{13}C NMR (101 MHz, Methanol-d_4) δ 151.2, 144.1, 131.2, 128.0, 127.2, 126.8, 126.2, 125.4, 125.2, 124.6, 119.5, 116.7, 34.1, 30.1. HRMS (ESI+) *m/z* calcd for $[C_{18}H_{20}N_2O_3]^+$: 312.37, found: 312.20. HPLC t_R = 11.586 min (97.6% purity).

3-(*tert*-butyl)-*N*-ethyl-*N*-(4-(hydroxycarbamoyl)phenyl)benzamide (2). ^{1}H NMR (700 MHz, Methanol-d_4) δ 7.64 (d, J = 8.5 Hz, 2H), 7.31 (dt, J = 7.5, 1.8 Hz, 1H), 7.22 – 7.14 (m, 5H), 4.00 (q, J = 7.1 Hz, 2H), 1.20 (t, J = 7.1 Hz, 3H), 1.10 (s, 9H). ^{13}C NMR (176 MHz, Methanol-d_4) δ 174.1, 168.1, 153.2, 148.7, 137.9, 133.1, 130.5, 130.3, 130.3, 129.3, 128.3, 128.2, 47.7, 36.7, 32.7, 14.3. HRMS (ESI+) *m/z* calcd for $[C_{20}H_{25}N_2O_3]$+: 341.18652, found: 341.18632, found: 341.18632. HPLC t_R = 19.045 min (>99% purity).

4-((3-(*tert*-butyl)-*N*-ethylphenyl)sulfonamido)-*N*-hydroxybenzamide (3). ^{1}H NMR (400 MHz, Acetonitrile-d_3) δ 7.75 – 7.70 (m, 3H), 7.54 – 7.47 (m, 2H), 7.41 (s, 1H), 7.15 (d, J = 8.3 Hz, 2H), 3.63 (q, J = 7.1 Hz, 2H), 1.26 (s, 9H), 1.03 (t, J = 7.1 Hz, 3H). ^{13}C NMR (101 MHz, Acetonitrile-d_3) δ 164.6, 152.5, 142.1, 137.4, 130.2, 129.0, 128.5, 127.6, 124.5, 124.2, 117.4, 45.0, 34.6, 30.2, 13.3. HRMS (ESI+) *m/z* calcd for $[C_{19}H_{25}N_2O_4S]$+: 377.1530, found: 377.1534. HPLC t_R = 21.260 min (99.4%).

***N*-ethyl-*N*-(4-(hydroxycarbamoyl)phenyl)-3-(trifluoromethyl)benzamide (4).** ^{1}H NMR (400 MHz, Acetonitrile-d_3) δ 7.67 – 7.58 (m, 4H), 7.53 (t, J = 7.4 Hz, 1H), 7.45 – 7.38 (m, 1H), 7.23, (d, J = 8.5 Hz, 2H), 4.77 (br, 2H), 3.97 (q, J = 7.1 Hz, 2H), 1.19 (t, J = 7.1 Hz, 3H). ^{13}C NMR (101 MHz, Acetonitrile-d_3) δ 168.2, 145.8, 137.5, 132.0, 128.9, 128.3, 128.2, 127.9, 126.8, 126.1, 125.3, 117.3, 45.0, 12.2. ^{19}F NMR (376 MHz, Acetonitrile-d_3) δ -63.42 (s, 3F). HRMS (ESI+) *m/z* calcd for [C17H16F3N2O3]+: 353.1108, found: 353.1109. HPLC t_R = 18.184 min (>99% purity).

4-((*N*-ethyl-3-(trifluoromethyl)phenyl)sulfonamido)-*N*-hydroxybenzamide (5). ^{1}H NMR (400 MHz, Acetone-d_6) δ 10.87 (br, 1H), 8.07 (d, J = 7.2 Hz, 1H), 7.94 – 7.81 (m, 5H), 7.26 (d, J = 8.6 Hz, 2H), 3.76 (q, J = 7.0 Hz, 2H), 1.09 (t, J = 7.1 Hz, 3H). ^{13}C NMR (101 MHz, Acetone-d_6) δ 205.3, 141.4, 139.6, 131.8, 131.3, 131.0, 130.7, 129.6, 128.6, 127.8, 126.1, 124.1, 45.3, 13.4. ^{19}F NMR (376 MHz, Acetone-d_6) δ -63.43 (s, 3F). HRMS (ESI+) *m/z* calcd for $[C_{16}H_{16}F_3N_2O_4S]$+: 389.0775, found: 389.0770. HPLC t_R = 20.241 min (>99% purity).

4-((*N*-ethyl-3,5-bis(trifluoromethyl)phenyl)sulfonamido)-*N*-hydroxybenzamide (6). ^{1}H NMR (400 MHz, Acetone-d_6) δ 10.90 (br, 1H), 8.43 (s, 1H), 8.14 – 8.09 (m, 2H), 7.90 (d, J = 8.6, 2H), 7.32 (d, J = 8.5, 2H), 3.81 (q, J = 7.1 Hz, 2H), 1.11 (t, J = 7.1 Hz, 3H). ^{13}C NMR (101 MHz, Acetone-d_6) δ 205.3, 141.0, 132.3, 128.9, 128.8, 127.9, 126.7, 126.3, 124.1, 121.4, 45.7, 13.3. ^{19}F NMR (376 MHz, Acetone-d_6) δ -63.52 (s, 6F). HRMS (ESI+) *m/z* calcd for $[C_{17}H_{15}F_6N_2O_4S]$+: 457.0649, found: 457.0644. HPLC t_R = 22.030 min (>99% purity).

3,5-di-*tert*-butyl-*N*-ethyl-*N*-(4-(hydroxycarbamoyl)phenyl)benzamide (7). ^{1}H NMR (400 MHz, Acetone-d_6) δ 10.56 (s, 1H), 7.70 (d, J = 8.5 Hz, 2H), 7.37 (t, J = 1.9 Hz, 1H), 7.20 (d, J = 8.5 Hz, 2H), 7.18 (d, J = 1.8 Hz, 2H), 3.99 (q, J = 7.1 Hz, 2H), 1.22 – 1.14 (m, 21H). ^{13}C NMR (101 MHz, Acetone-d_6) δ 205.9, 170.0, 150.1, 146.9, 135.5, 127.9, 127.6, 123.4, 123.2, 117.0, 44.7, 34.4, 30.5, 12.4. HRMS (ESI+) *m/z* calcd for $[C_{24}H_{33}N_2O_3]$+: 397.2486, found: 397.2487. HPLC t_R = 22.814 min (>99% purity).

***N*-(3,5-di-*tert*-butylbenzyl)-*N*-(4-(hydroxycarbamoyl)phenyl)-3-(trifluoromethyl)benzamide**

(8). ^{1}H NMR (400 MHz, Acetone-d_6) δ 7.76 – 7.58 (m, 5H), 7.52 – 7.43 (m, 1H), 7.37 (s, 1H), 7.22 – 7.20, 7.12 (m, 4H), 5.24 (s, 2H), 1.28 (s, 18H). ^{13}C NMR (101 MHz, Acetone-d_6) δ 205.3, 168.3, 150.7, 145.9, 137.5, 136.4, 132.3, 130.2, 129.9, 129.5, 129.0, 127.9, 127.7, 126.3, 125.4, 122.4, 121.0, 53.5, 34.4, 30.8. ^{19}F NMR (376 MHz, Acetone-d_6) δ -63.35 (s, 3F). HRMS (ESI+) *m/z* calcd for $[C_{30}H_{34}F_3N_2O_3]$+: 527.2516, found: 527.2518. HPLC t_R = 28.483 min (>99% purity).

***N*-(4-(hydroxycarbamoyl)phenyl)-3-(trifluoromethyl)-*N*-(3-(trifluoromethyl)benzyl)benzamide (9).** ^{1}H NMR (700 MHz, Methanol-d_4) δ 7.66 (s, 1H), 7.60 – 7.56 (m, 6H), 7.54 (d, *J* = 7.7 Hz, 1H), 7.48 (t, *J* = 7.7 Hz, 1H), 7.41 (t, *J* = 7.8 Hz, 1H), 7.14 (d, *J* = 8.6 Hz, 2H), 5.28 (s, 2H).^{13}C NMR (176 MHz, Methanol-d_4) δ 172.3, 168.0, 147.7, 140.6, 139.0, 134.6, 133.7, 132.9, 131.8, 131.4, 130.6, 130.5, 129.1, 129.0, 127.9, 127.6, 127.0, 126.8, 126.0, 125.5, 55.3. ^{19}F NMR (658 MHz, Methanol-d_4) δ -64.24 (s, 3F), -64.50 (s, 3F). HRMS (ESI+) *m/z* calcd for $[C_{23}H_{17}F_6N_2O_3]$+: 483.1147, found: 483.1144. HPLC t_R = 23.546 min (>99% purity).

***N*-benzyl-*N*-(4-(hydroxycarbamoyl)phenyl)-3-(trifluoromethyl)benzamide (10).** ^{1}H NMR (700 MHz, Methanol-d_4) δ 7.66 (s, 1H), 7.60 – 7.50 (m, 4H), 7.36 (t, *J* = 7.8 Hz, 1H), 7.28 (d, *J* = 7.3 Hz, 2H), 7.24 (t, *J* = 7.3 Hz, 2H), 7.20 (t, *J* = 7.3 Hz, 1H), 7.10 (d, *J* = 8.4 Hz, 2H), 5.18 (s, 2H). ^{13}C NMR (176 MHz, Methanol-d_4) δ 172.2, 168.1, 147.9, 139.3, 139.2, 134.6, 133.5, 132.7, 131.4, 130.9, 130.8, 130.7, 130.4, 130.0, 129.0, 127.9, 126.3, 55.8. ^{19}F NMR (658 MHz, Methanol-d_4) δ -64.22 (s, 3F). HRMS (ESI+) *m/z* calcd for $[C_{22}H_{18}F_3N_2O_3]$+: 415.1273, found: 415.1275. HPLC t_R = 22.033 min (>99% purity).

***N*-(4-(hydroxycarbamoyl)phenyl)-3-(trifluoromethyl)benzamide (11).** ^{1}H NMR (700 MHz, Methanol-d_4) δ 8.24 (s, 1H), 8.19 (d, *J* = 7.8 Hz, 1H), 7.87 (d, *J* = 7.7 Hz, 1H), 7.84 (d, *J* = 8.7 Hz, 2H), 7.76 (d, *J* = 8.7 Hz, 2H), 7.71 (t, *J* = 7.8 Hz, 1H). ^{13}C NMR (176 MHz, Methanol-d_4) δ 168.9, 168.4, 144.3, 138.3, 133.6, 133.3, 131.9, 130.7, 130.4, 130.2, 126.9, 126.6, 122.8. ^{19}F NMR (658 MHz, Methanol-d_4) δ -64.22 (s, 3F). HRMS (ESI+) *m/z* calcd for $[C_{15}H_{12}F_3N_2O_3]$+: 325.0795, found: 325.0794. HPLC t_R = 10.522 min (>99% purity).

***N*-ethyl-*N*-(4-(hydroxycarbamoyl)phenyl)-2-(trifluoromethyl)benzamide (12).** ^{1}H NMR (700 MHz, Methanol-d_4) δ 7.61 (d, *J* = 8.47 Hz, 2H), 7.59 (d, *J* = 7.7 Hz, 1H), 7.40 – 7.33 (m, 2H), 7.26 – 7.24 (m, 3H), 3.99 (br, 2H), 1.22 (t, *J* = 7.2 Hz, 3H). ^{13}C NMR (176 MHz, Methanol-d_4) δ 171.0, 168.1, 147.1, 137.1, 134.1, 134.0, 131.9, 131.4, 130.9, 130.5, 129.7, 129.0, 126.6, 47.1, 14.1. ^{19}F NMR (658 MHz, Methanol-d_4) δ -59.94 (s, 3F). HRMS (ESI+) *m/z* calcd for $[C_{17}H_{16}F_3N_2O_3]$+: 353.1108, found: 353.1107. HPLC t_R = 9.442 min (>99% purity).

***N*-hydroxy-4-(*N*-(3-(trifluoromethyl)benzyl)acetamido)benzamide (13).** ^{1}H NMR (700 MHz, Methanol-d_4) δ 7.76 (d, *J* = 8.4 Hz, 2H), 7.53 (d, *J* = 7.2 Hz, 1H), 7.49 (s, 1H), 7.48 – 7.43 (m, 2H), 7.23 (d, *J* = 8.4 Hz, 2H), 5.01 (s, 2H), 1.92 (s, 3H). ^{13}C NMR (176 MHz, Methanol-d_4) δ 174.0, 168.2, 147.6, 141.0, 134.7, 134.6, 133.1, 131.7, 130.9, 130.7, 127.5, 126.6, 126.0, 54.4, 23.9. ^{19}F NMR (658 MHz, Methanol-d_4) δ -64.21 (s, 3F). HRMS (ESI+) *m/z* calcd for $[C_{17}H_{16}F_3N_2O_3]$+: 353.1108, found: 353.1108. HPLC t_R = 18.616 min (98.3% purity).

4-(*N*-(3,5-bis(trifluoromethyl)benzyl)acetamido)-*N*-hydroxybenzamide (14). ^{1}H NMR (700 MHz, Methanol-d_4) δ 7.84 (s, 1H), 7.84 – 7.77 (m, 4H), 7.26 (d, *J* = 8.5 Hz, 2H), 5.09 (s, 2H), 1.94 (s, 3H). ^{13}C NMR (176 MHz, Methanol-d_4) δ 174.2, 168.1, 147.4, 143.1 134.9, 134.1, 131.4, 131.1, 130.6, 125.9, 123.6, 54.1, 23.8. ^{19}F NMR (658 MHz, Methanol-d_4) δ -64.44 (s, 6F). HRMS (ESI+) *m/z* calcd for $[C_{18}H_{15}F_6N_2O_3]$+: 421.0979, found: 421.0978. HPLC t_R = 20.187 min (98.6% purity).

***N*-(cyclopropylmethyl)-*N*-(4-(hydroxycarbamoyl)phenyl)-3-(trifluoromethyl)benzamide (15).** ^{1}H NMR (700 MHz, Methanol-d_4) δ 7.67 (d, *J* = 8.5 Hz, 2H), 7.61 (s, 1H), 7.56 (d, *J* = 7.9 Hz, 1H), 7.52 (d, *J* = 7.8 Hz, 1H), 7.39 (t, *J* = 7.8 Hz, 1H), 7.29 (d, *J* = 8.5 Hz, 2H), 3.84 (d, *J* = 7.2 Hz, 2H), 1.11 – 1.04 (m, 1H), 0.48 – 0.41 (m, 2H), 0.18 – 0.12 (m, 2H). ^{13}C NMR (176 MHz, Methanol-d_4) δ 172.1, 168.2, 148.5, 139.6, 134.4, 133.6, 132.7, 131.3, 131.0, 130.5, 128.7, 127.7, 126.3, 57.1, 11.9, 5.5. ^{19}F NMR (658 MHz, Methanol-d_4) δ -64.38 (s, 3F). HRMS (ESI+) *m/z* calcd for $[C_{19}H_{18}F_3N_2O_3]$+: 379.1262, found: 379.1259. HPLC t_R = 21.253 min (>99% purity).

***N*-(4-(hydroxycarbamoyl)phenyl)-*N*-isopropyl-3-(trifluoromethyl)benzamide (16).** ^{1}H NMR (700 MHz, Methanol-d_4) δ 7.66 (d, *J* = 8.3 Hz, 2H), 7.57 (s, 1H), 7.50 (t, *J* = 7.7 Hz, 2H), 7.36 (t, *J* = 7.9 Hz, 1H), 7.27 (d, *J* = 8.3 Hz, 2H), 4.99 (br, 1H), 1.23 (d, *J* = 6.9 Hz, 6H). ^{13}C NMR (176 MHz, Methanol-d_4) δ 172.3, 168.1, 144.5, 140.5, 134.4, 133.9, 133.4, 132.6, 131.2, 130.1, 128.3, 127.2, 126.4, 51.3, 22.4. ^{19}F NMR (658 MHz, Methanol-d_4) δ -64.37 (s, 3F). HRMS (ESI+) *m/z* calcd for $[C_{18}H_{18}F_3N_2O_3]$+: 367.1264, found: 367.1263. HPLC t_R = 20.680 min (>99% purity).

3-(*tert*-butyl)-*N*-(cyclopropylmethyl)-*N*-(4-(hydroxycarbamoyl)phenyl)benzamide (MMH371). ^{1}H NMR (700 MHz, Methanol-d_4) δ 7.64 (d, *J* = 8.6 Hz, 2H), 7.30 (dt, *J* = 7.6, 1.7 Hz, 1H), 7.23 (d, *J* = 8.6 Hz, 2H), 7.22 – 7.19 (m, 2H), 7.17 (t, *J* = 7.6 Hz, 1H), 3.84 (d, *J* = 7.1 Hz, 2H), 1.11 (s, 9H), 1.09 – 1.05 (m, 1H), 0.46 – 0.42 (m, 2H), 0.14 (q, *J* = 5.2 Hz, 2H). ^{13}C NMR (176 MHz, Methanol-d_4) δ 174.3, 168.1, 153.2, 149.3, 137.9, 133.1, 130.8, 130.28, 130.27, 129.2, 128.3, 128.2, 57.0, 36.7, 32.7, 12.0, 5.4. HRMS (ESI+) *m/z* calcd for $[C_{22}H_{27}N_2O_3]$+: 367.1943, found: 367.2016. HPLC t_R = 27.958 min (>99% purity).

3,5-di-*tert*-butyl-*N*-(cyclopropylmethyl)-*N*-(4-(hydroxycarbamoyl)phenyl)benzamide (17). ^{1}H NMR (700 MHz, Methanol-d_4) δ 7.66 (d, *J* = 8.3 Hz, 2H), 7.33 (s, 1H), 7.22 (d, *J* = 8.1 Hz, 2H), 7.14 (s, 2H), 3.85 (d, *J* = 7.2 Hz, 2H), 1.15 (s, 18H), 0.43 (q, *J* = 7.9 Hz, 2H), 0.14 (q, *J* = 5.2 Hz, 2H). ^{13}C NMR (176 MHz, Methanol-d_4) δ 174.6, 168.0, 153.0, 149.6, 137.3, 132.9, 130.7, 130.3, 126.1, 125.8, 57.0, 36.9, 32.9, 12.0, 5.5. HRMS (ESI+) *m/z* calcd for $[C_{26}H_{35}N_2O_3]$+: 423.2642, found: 423.2636. HPLC t_R = 34.486 min (>99% purity).

3,5-di-*tert*-butyl-*N*-(cyclopropylmethyl)-*N*-(4-(hydroxycarbamoyl)phenyl)benzamide (18). ^{1}H NMR (700 MHz, Methanol-d_4) δ 7.85-7.80 (m, 2H), 7.79 – 7.73 (m, 4H), 7.69 – 7.65 (m, 1H), 1.37 (s, 18H). ^{13}C NMR (176 MHz, Methanol-d_4) δ 171.3, 169.0, 153.8, 144.6, 136.8, 130.1, 130.1, 128.6, 124.2, 122.9, 37.2, 33.0. HRMS (ESI+) *m/z* calcd for $[C_{22}H_{29}N_2O_3]$+: 369.2173, found: 369.2172. HPLC t_R = 35.032 min (>99% purity).

***N*-(4-(hydroxycarbamoyl)phenyl)-*N*-isopropyl-3,5-bis(trifluoromethyl)benzamide (MMH409).** ^{1}H NMR (700 MHz, Methanol-d_4) δ 7.85 (s, 2H), 7.80 (s, 1H), 7.70 (d, *J* = 8.2

Hz, 2H), 7.33 (d, J = 8.2 Hz, 2H), 5.02 (br, 1H), 1.24 (d, J = 7.1 Hz, 6H). ^{13}C NMR (176 MHz, Methanol-d_4) δ 170.3, 167.9, 144.2, 141.9, 134.7, 133.6, 133.5, 131.0, 130.3, 125.5, 125.1, 51.4, 22.3. ^{19}F NMR (658 MHz, Methanol-d_4) δ -64.52 (s, 6F). HRMS (ESI+) *m/z* calcd for $[C_{19}H_{17}F_6N_2O_3]$+: 435.1138, found: 435.1131. HPLC t_R = 28.875 min (>99% purity).

***N*-(4-(hydroxycarbamoyl)phenyl)-*N*-isopropyl-3-(trifluoromethoxy)benzamide (MMH410)**. ^{1}H NMR (700 MHz, Methanol-d_4) δ 7.66 (d, J = 8.4 Hz, 2H), 7.31 – 7.22 (m, 4H), 7.15 (s, 1H), 7.12 (d, J = 7.7 Hz, 1H), 4.97 (br, 1H), 1.22 (d, J = 6.9 Hz, 6H). ^{13}C NMR (176 MHz, Methanol-d_4) δ 172.1, 168.1, 151.0, 144.5, 141.6, 134.4, 133.3, 132.2, 130.1, 129.1, 124.3, 123.0, 122.9, 51.3, 22.4. ^{19}F NMR (658 MHz, Methanol-d_4) δ -59.61 (s, 3F). HRMS (ESI+) *m/z* calcd for $[C_{18}H_{18}F_3N_2O_4]$+: 383.1211, found: 383.1209. HPLC t_R = 18.415 min (>99% purity).

2-fluoro-*N*-(4-(hydroxycarbamoyl)phenyl)-*N*-isopropyl-3-(trifluoromethyl)benzamide (19). ^{1}H NMR (700 MHz, Methanol-d_4) δ 7.64 (d, J = 8.1 Hz, 2H), 7.52 (dt, J = 28.4, 7.1 Hz, 2H), 7.27 (d, J = 8.1 Hz, 2H), 7.17 (t, J = 7.8 Hz, 1H), 5.04 (h, J = 6.7 Hz, 1H), 1.22 (d, J = 7.0 Hz, 6H). ^{13}C NMR (176 MHz, Methanol-d_4) δ 168.0, 167.7, 157.9, 156.4, 143.2, 135.7, 135.0, 133.0, 130.2, 130.0, 126.9, 124.9, 120.5, 50.8, 22.3. ^{19}F NMR (658 MHz, Methanol-d_4) δ -63.05 (d, J = 12.6 Hz, 3F), -118.30 – -118.44 (m, 1F). HRMS (ESI+) *m/z* calcd for $[C_{18}H_{17}F_4N_2O_3]$+: 385.1170, found: 385.1171. HPLC t_R = 18.324 min (>99% purity).

4-fluoro-*N*-(4-(hydroxycarbamoyl)phenyl)-*N*-isopropyl-3-(trifluoromethyl)benzamide (20). ^{1}H NMR (700 MHz, Methanol-d_4) δ 7.68 (d, J = 8.4 Hz, 2H), 7.62 (d, J = 6.3 Hz, 1H), 7.56 – 7.52 (br, 1H), 7.27 (d, J = 8.4 Hz, 2H), 7.13 (t, J = 9.5 Hz, 1H), 4.97 (br, 1H), 1.23 (d, J = 6.9 Hz, 6H). ^{13}C NMR (176 MHz, Methanol-d_4) δ 171.2, 168.1, 144.6, 136.9, 136.3, 134.5, 133.3, 130.2, 129.8, 124.8, 120.0, 119.1, 119.0, 51.5, 22.3. ^{19}F NMR (658 MHz, Methanol-d_4) δ -63.10 (d, J = 12.7 Hz, 3F), -114.56 – -114.67 (m, 1F). HRMS (ESI+) *m/z* calcd for $[C_{18}H_{17}F_4N_2O_3]$+: 385.1167, found: 385.1166. HPLC t_R = 18.703 min (>99% purity).

3,5-di-*tert*-butyl-*N*-(4-(hydroxycarbamoyl)phenyl)-*N*-isopropylbenzamide (21). ^{1}H NMR (700 MHz, Methanol-d_4) δ 7.65 (d, J = 8.4 Hz, 2H), 7.28 (s, 1H), 7.20 (d, J = 8.4 Hz, 2H), 7.08 (s, 2H), 4.99 (br, 1H), 1.24 (d, J = 6.8 Hz, 6H), 1.16 (s, 18H). ^{13}C NMR (176 MHz, Methanol-d_4) δ 174.8, 168.0, 152.9, 145.6, 138.3, 133.8, 133.2, 129.9, 125.6, 125.1, 51.2, 36.9, 32.9, 22.5. HRMS (ESI+) *m/z* calcd for $[C_{25}H_{35}N_2O_3]$+: 411.2642, found: 411.2642. HPLC t_R = 23.806 min (>99% purity).

***N*-(4-(hydroxycarbamoyl)phenyl)-3,5-bis(trifluoromethyl)benzamide (22).** ^{1}H NMR (700 MHz, Methanol-d_4) δ 8.55 (s, 2H), 8.20 (s, 1H), 7.86 (d, J = 8.7 Hz, 2H), 7.82 – 7.75 (d, J = 8.7 Hz, 2H). ^{13}C NMR (176 MHz, Methanol-d_4) δ 168.9, 166.6, 144.1, 139.8, 134.4, 130.7, 130.2, 127.5, 125.8, 122.8. ^{19}F NMR (564 MHz, Methanol-d_4) δ -64.38 (s, 6F). HRMS (ESI+) *m/z* calcd for $[C_{16}H_{11}F_6N_2O_3]$+: 393.0677, found: 393.0675. HPLC t_R = 20.396 min (98.2% purity).

***N*^{1}-(3-(*tert*-butyl)phenyl)-*N*^{4}-hydroxyterephthalamide (23).** ^{1}H NMR (700 MHz, Methanol-d_4) δ 7.99 (d, J = 8.3 Hz, 2H), 7.85 (d, J = 8.3 Hz, 2H), 7.74 (s, 1H), 7.52 (d, J = 7.0 Hz, 1H), 7.27 (t, J = 7.9 Hz, 1H), 7.20 (ddd, J = 7.8, 1.9, 1.0 Hz, 1H), 1.32 (s, 9H). ^{13}C NMR (176 MHz, Methanol-d_4) δ 169.1, 168.4, 154.4, 140.6, 140.5, 137.7, 130.7, 130.1, 129.6, 124.1, 120.79, 120.77, 36.9, 33.0. HRMS (ESI+) *m/z* calcd for [C18H21N2O3]+: 313.1547, found: 313.1545. HPLC t_R = 27.776 min (>99% purity).

***N*^{1}-(3-(*tert*-butyl)phenyl)-*N*^{1}-ethyl-*N*^{4}-hydroxyterephthalamide (24).** ^{1}H NMR (700 MHz, Methanol-d_4) δ 7.55 (d, J = 7.7 Hz, 2H), 7.31 (d, J = 8.0 Hz, 2H), 7.23 – 7.16 (m, 2H), 7.05 – 6.93 (m, 2H), 4.00 – 3.96 (br, 2H), 1.21 (t, J = 7.2 Hz, 3H), 1.12 (s, 9H). ^{13}C NMR (176 MHz, Methanol-d_4) δ 172.9, 168.2, 155.1, 144.6, 142.3, 135.5, 131.4, 130.8, 128.9, 128.7, 126.9, 126.4, 47.4, 36.6, 32.7, 14.3. HRMS (ESI+) *m/z* calcd for $[C_{20}H_{25}N_2O_3]$+: 341.1860, found: 341.1856. HPLC t_R = 27.544 min (>99% purity).

ASSOCIATED CONTENT

Supporting Information

The Supporting Information is available free of charge on the ACS Publications website at DOI:

Additional figures and tables illustrating the HDAC binding and inhibition profiles using FP, EMSA, SPR, and TSA; additional tables summarizing PAMPA, and *in vivo* pharmacokinetic (PK) results of selected compounds from the SAR; additional figures and tables illustrating the L-shape of inhibitors using two-dimensional NOESY experiments, DFT, and docking experiments; additional figures indicating the existence of a conformational equilibrium using variable-temperature one-dimensional NMR experiments; additional figures demonstrating the cellular HDAC8-target engagement using immunofluorescence and western blotting; compound characterization data (PDF)

X-ray crystallographic data (CIF)

AUTHOR INFORMATION

Corresponding Author

*patrick.gunning@utoronto.ca

Notes

All animal experiments performed in the manuscript were in compliance with institutional guidelines.

ACKNOWLEDGMENT

P.T.G. is thankful for the financial support from research grants such as NSERC (RGPIN-2014-05767), CIHR (MOP-130424, MOP-137036), Canada Research Chair (950-232042), Canadian Cancer Society (703963), Canadian Breast Cancer Foundation (705456), infrastructure grants from CFI (33536), and the Ontario Research Fund (34876).

ABBREVIATIONS

HDAC, histone deacetylase; HDACi, HDAC inhibitor; PAMPA, parallel artificial membrane permeability assay; FP, fluorescence polarization; SPR, surface plasmon resonance; TLC, thin layer chromatography; LRMS, low-resolution mass spectrometry; HRMS, high-resolution mass spectrometry; NMR, nuclear magnetic resonance; NOE, nuclear Overhauser effect; NOESY, nuclear Overhauser effect spectroscopy; PK, pharmacokinetic; DFT, density functional theory; Ac, acetylated; SMC3, Structural

Maintenance of Chromosomes protein 3; IC_{50}, half maximal inhibitory concentration.

REFERENCES

(1) Ropero, S.; Esteller, M. The Role of Histone Deacetylases (HDACs) in Human Cancer. *Mol. Oncol.* **2007**, *1*, 19–25.

(2) Seto, E.; Yoshida, M. Erasers of Histone Acetylation : The Histone Deacetylase Enzymes. *Cold Spring Harb Perspect Biol* **2014**, *6*, 1–26.

(3) Rettig, I.; Koeneke, E.; Trippel, F.; Mueller, W. C.; Burhenne, J.; Fabian, J.; Schober, A.; Fernekorn, U.; Deimling, A. Von; Deubzer, H. E.; Milde, T.; Witt, O.; Oehme, I. Selective Inhibition of HDAC8 Decreases Neuroblastoma Growth in Vitro and in Vivo and Enhances Retinoic Acid-Mediated Differentiation. *Cell Death Dis.* **2015**, *6*, e1657.

(4) Ramos, T. L.; Sánchez-abarca, L. I.; Redondo, A.; Almeida, A. M.; Puig, N.; Ortega, R.; Preciado, S.; Rico, A.; Muntión, S. HDAC8 Overexpression in Mesenchymal Stromal Cells from JAK2+myeloproliferative Neoplasms: A New Therapeutic Target? *Oncotarget* **2017**, *8*, 28187–28202.

(5) Hassan, M. M.; Olaoye, O. O. Recent Advances in Chemical Biology Using Benzophenones and Diazirines as Radical Precursors. *Molecules* **2020**, *25*, 2285.

(6) Mariadason, J. M. Making Sense of HDAC2 Mutations in Colon Cancer. *Gastroenterology* **2008**, *135*, 1457–1459.

(7) Huang, B. H.; Laban, M.; Leung, C.; Lee, L.; Lee, C. K.; Raju, G. C.; Hooi, S. C. Inhibition of Histone Deacetylase 2 Increases Apoptosis and P21 Cip1 / WAF1 Expression , Independent of Histone Deacetylase 1. *Cell Death Differ.* **2005**, *12*, 395–404.

(8) Barneda-Zahonero, B.; Parra, M. Histone Deacetylases and Cancer. *Mol. Oncol.* **2012**, *6*, 579–589.

(9) Oehme, I.; Deubzer, H. E.; Lodrini, M.; Milde, T.; Witt, O. Targeting of HDAC8 and Investigational Inhibitors in Neuroblastoma. *Expert Opin. Investig. Drugs* **2009**, *18*, 1605–1617.

(10) Yoon, S.; Eom, G. H. HDAC and HDAC Inhibitor : From Cancer to Cardiovascular Diseases. *Chonnam Med. J.* **2016**, *52*, 1–11.

(11) Hyun-Jung, K.; Suk-Chul, B. Histone Deacetylase Inhibitors: Molecular Mechanisms of Action and Clinical Trials as Anti-Cancer Drugs. *Am J Transl Res* **2011**, *3*, 166–179.

(12) Joanna, F.; A, V. G. L.; Mathieu, V.; Sarah, S.; Sarah, D.; Karin, V.; Tamara, V.; Vera, R. Histone Deacetylase Inhibition and the Regulation of Cell Growth with Particular Reference to Liver Pathobiology. *J. Cell. Mol. Med.* **2009**, *13*, 2990–3005.

(13) Li, T.; Zhang, C.; Hassan, S.; Liu, X.; Song, F.; Chen, K.; Zhang, W. Histone Deacetylase 6 in Cancer. **2018**, *1*, 1–10.

(14) Ceccacci, E.; Minucci, S. Inhibition of Histone Deacetylases in Cancer Therapy: Lessons from Leukaemia. *Br. J. Cancer* **2016**, *114*, 605–611.

(15) Zhang, S. L.; Zhu, H. Y.; Zhou, B. Y.; Chu, Y.; Huo, J. R.; Tan, Y. Y.; Liu, D. L. Histone Deacetylase 6 Is Overexpressed and Promotes Tumor Growth of Colon Cancer through Regulation of the MAPK/ERK Signal Pathway. *Onco. Targets. Ther.* **2019**, *12*, 2409–2419.

(16) Song, S.; Wang, Y.; Xu, P.; Yang, R.; Ma, Z.; Liang, S.; Zhang, G. The Inhibition of Histone Deacetylase 8 Suppresses Proliferation and Inhibits Apoptosis in Gastric Adenocarcinoma. *Int. J. Oncol.* **2015**, *47*, 1819–1828.

(17) Thaler, F.; Mercurio, C. Towards Selective Inhibition of Histone Deacetylase Isoforms: What Has Been Achieved, Where We Are and What Will Be Next. *ChemMedChem* **2014**, *9*, 523–536.

(18) Bieliauskas, A. V.; Pflum, M. K. H. Isoform-Selective Histone Deacetylase Inhibitors. *Chem. Soc. Rev.* **2008**, *37*, 1402–1413.

(19) Hsu, K. C.; Liu, C. Y.; Lin, T. E.; Hsieh, J. H.; Sung, T. Y.; Tseng, H. J.; Yang, J. M.; Huang, W. J. Novel Class IIa-Selective Histone Deacetylase Inhibitors Discovered Using an in Silico Virtual Screening Approach. *Sci. Rep.* **2017**, *7*, 1–13.

(20) Dallavalle, S.; Pisano, C.; Zunino, F. Development and Therapeutic Impact of HDAC6-Selective Inhibitors. *Biochem. Pharmacol.* **2012**, *84*, 756–765.

(21) Marek, M.; Shaik, T. B.; Heimburg, T.; Chakrabarti, A.; Lancelot, J.; Ramos-Morales, E.; Da Veiga, C.; Kalinin, D.; Melesina, J.; Robaa, D.; Schmidtkunz, K.; Suzuki, T.; Holl, R.; Ennifar, E.; Pierce, R. J.; Jung, M.; Sippl, W.; Romier, C. Characterization of Histone Deacetylase 8 (HDAC8) Selective Inhibition Reveals Specific Active Site Structural and Functional Determinants. *J. Med. Chem.* **2018**, *61*, 10000–10016.

(22) Shouksmith, A. E.; Gawel, J. M.; Nawar, N.; Sina, D.; Raouf, Y. S.; Bukhari, S.; He, L.; Johns, A. E.; Manaswiyoungkul, P.; Olaoye, O. O.; Cabral, A. D.; Sedighi, A.; de Araujo, E. D.; Gunning, P. T. Class I/IIb-Selective HDAC Inhibitor Exhibits Oral Bioavailability and Therapeutic Efficacy in Acute Myeloid Leukemia. *ACS Med. Chem. Lett.* **2020**, *11*, 56–64.

(23) Hirano, T.; Osaki, T.; Fujii, S.; Komatsu, D.; Azumaya, I.; Tanatani, A. Fluorescent Visualization of the Conformational Change of Aromatic Amide or Urea Induced by N-Methylation. *Tetrahedron Lett.* **2009**, *50*, 488–491.

(24) Talele, T. T. The "Cyclopropyl Fragment" Is a Versatile Player That Frequently Appears in Preclinical/Clinical Drug Molecules. *J. Med. Chem.* **2016**, *59*, 8712–8756.

(25) De Vreese, R.; D'hooghe, M. Synthesis and Applications of Benzohydroxamic Acid-Based Histone Deacetylase Inhibitors. *Eur. J. Med. Chem.* **2017**, *135*, 174–195.

(26) Zhao, C.; Zang, J.; Ding, Q.; Inks, E. S.; Xu, W.; Chou, C. J.; Zhang, Y. Discovery of Meta-Sulfamoyl N-Hydroxybenzamides as HDAC8 Selective Inhibitors. *Eur. J. Med. Chem.* **2018**, *150*, 282–291.

(27) Heimburg, T.; Chakrabarti, A.; Lancelot, J.; Marek, M.; Melesina, J.; Hauser, A. T.; Shaik, T. B.; Duclaud, S.; Robaa, D.; Erdmann, F.; Schmidt, M.; Romier, C.; Pierce, R. J.; Jung, M.; Sippl, W. Structure-Based Design and Synthesis of Novel Inhibitors Targeting HDAC8 from Schistosoma Mansoni for the Treatment of Schistosomiasis. *J. Med. Chem.* **2016**, *59*, 2423–2435.

(28) Ralph Mazitschek, Vishal Patelb, Dyann F. Wirth, and J. C. Development of a Fluorescence Polarization Based Assay for Histone Deacetylase Ligand Discovery.

Bioorg Med Chem Lett. **2008**, *18*, 2809–2812.

(29) Brunsteiner, M.; Petukhov, P. A. Insights from Comprehensive Multiple Receptor Docking to HDAC8. *J. Mol. Model.* **2012**, *18*, 3927–3939.

(30) Deschamps, N.; Simões-Pires, C. A.; Carrupt, P. A.; Nurisso, A. How the Flexibility of Human Histone Deacetylases Influences Ligand Binding: An Overview. *Drug Discov. Today* **2015**, *20*, 736–742.

(31) Tiwary, P.; Limongelli, V.; Salvalaglio, M.; Parrinello, M. Kinetics of Protein-Ligand Unbinding: Predicting Pathways, Rates, and Rate-Limiting Steps. *Proc. Natl. Acad. Sci. U. S. A.* **2015**, *112*, E386–E391.

(32) Bernetti, M.; Masetti, M.; Rocchia, W.; Cavalli, A. Kinetics of Drug Binding and Residence Time. *Annu. Rev. Phys. Chem.* **2019**, *70*, 143–171.

(33) Futamura, M.; Dhanasekaran, P.; Handa, T.; Phillips, M. C.; Lund-Katz, S.; Saito, H. Two-Step Mechanism of Binding of Apolipoprotein E to Heparin: Implications for the Kinetics of Apolipoprotein E-Heparan Sulfate Proteoglycan Complex Formation on Cell Surfaces. *J. Biol. Chem.* **2005**, *280*, 5414–5422.

(34) Chabaud, L.; Clayden, J.; Helliwell, M.; Page, A.; Raftery, J.; Vallverdú, L. Conformational Studies of Tertiary Oligo-m-Benzanilides and Oligo-p-Benzanilides in Solution. *Tetrahedron* **2010**, *66*, 6936–6957.

(35) Okamoto, I.; Nabeta, M.; Yamamoto, M.; Mikami, M.; Takeya, T.; Tamura, O. Solvent-Dependent Conformational Switching of the Aromatic N-Methyl Amides Depending upon the Acceptor Properties of Solvents. *Tetrahedron Lett.* **2006**, *47*, 7143–7146.

(36) Azumaya, I.; Kagechika, H.; Fujiwara, Y.; Itoh, M.; Yamaguchi, K.; Shudo, K.; Fujiwara, Y.; Itoh, M.; Yamaguchi, K. Twisted Intramolecular Charge-Transfer Fluorescence of Aromatic Amides: Conformation of the Amide Bonds in the Excited States. *J. Am. Chem. Soc.* **1991**, *113*, 2833–2838.

(37) Okamoto, I.; Nabeta, M.; Minami, T.; Nakashima, A.; Morita, N.; Takeya, T.; Masu, H.; Azumaya, I.; Tamura, O. Acid-Induced Conformational Switching of Aromatic N-Methyl-N-(2-Pyridyl)Amides. *Tetrahedron Lett.* **2007**, *48*, 573–577.

(38) Itai, A.; Toriumi, Y.; Tomioka, N.; Kagechika, H.; Azumaya, I.; Shudo, K. Stereochemistry of N-Methylbenzanilide and Benzanilide. *Tetrahedron Lett.* **1989**, *30* , 6177–6180.

(39) Okamoto, I.; Nabeta, M.; Hayakawa, Y.; Morita, N.; Takeya, T.; Masu, H.; Azumaya, I.; Tamura, O. Acid-Induced Molecular Folding and Unfolding of N-Methyl Aromatic Amide Bearing 2,6-Disubstituted Pyridines. *J. Am. Chem. Soc.* **2007**, *129*, 1892–1893.

(40) Friesner, R. A.; Murphy, R. B.; Repasky, M. P.; Frye, L. L.; Greenwood, J. R.; Halgren, T. A.; Sanschagrin, P. C.; Mainz, D. T. Extra Precision Glide: Docking and Scoring Incorporating a Model of Hydrophobic Enclosure for Protein-Ligand Complexes. *J. Med. Chem.* **2006**, *49*, 6177–6196.

(41) Friesner, R. A.; Banks, J. L.; Murphy, R. B.; Halgren, T. A.; Klicic, J. J.; Mainz, D. T.; Repasky, M. P.; Knoll, E. H.; Shelley, M.; Perry, J. K.; Shaw, D. E.; Francis, P.; Shenkin, P. S. Glide: A New Approach for Rapid, Accurate Docking and Scoring. 1. Method and Assessment of Docking Accuracy. *J. Med. Chem.* **2004**, *47*, 1739–1749.

(42) Halgren, T. A.; Murphy, R. B.; Friesner, R. A.; Beard, H. S.; Frye, L. L.; Pollard, W. T.; Banks, J. L. Glide: A New Approach for Rapid, Accurate Docking and Scoring. 2. Enrichment Factors in Database Screening. *J. Med. Chem.* **2004**, *47*, 1750–1759.

(43) Shouksmith, A. E.; Shah, F.; Grimard, M. L.; Gawel, J. M.; Raouf, Y. S.; Geletu, M.; Berger-Becvar, A.; De Araujo, E. D.; Luchman, H. A.; Heaton, W. L.; Bakhshinyan, D.; Adile, A. A.; Venugopal, C.; O'Hare, T.; Deininger, M. W.; Singh, S. K.; Konieczny, S. F.; Weiss, S.; Fishel, M. L.; Gunning, P. T. Identification and Characterization of AES-135, a Hydroxamic Acid-Based HDAC Inhibitor That Prolongs Survival in an Orthotopic Mouse Model of Pancreatic Cancer. *J. Med. Chem.* **2019**, *62*, 2651–2665.

(44) Chakrabarti, A.; Oehme, I.; Witt, O.; Oliveira, G.; Sippl, W.; Romier, C.; Pierce, R. J.; Jung, M. HDAC8 : A Multifaceted Target for Therapeutic Interventions. *Trends Pharmacol. Sci.* **2015**, *36*, 481–492.

(45) Brodeur, G. M. Neuroblastoma: Biological Insights into a Clinical Enigma. *Nat. Rev. Cancer* **2003**, *3*, 203–216.

(46) Dasgupta, T.; Antony, J.; Braithwaite, A. W.; Horsfield, J. A. HDAC8 Inhibition Blocks SMC3 Deacetylation and Delays Cell Cycle Progression without Affecting Cohesin-Dependent Transcription in MCF7 Cancer Cells. *J. Biol. Chem.* **2016**, *291*, 12761–12770.

(47) Emmons, M. F.; Faião-Flores, F.; Sharma, R.; Thapa, R.; Messina, J. L.; Becker, J. C.; Schadendorf, D.; Seto, E.; Sondak, V. K.; Koomen, J. M.; Chen, Y. A.; Lau, E. K.; Wan, L.; Licht, J. D.; Smalley, K. S. M. HDAC8 Regulates a Stress Response Pathway in Melanoma to Mediate Escape from BRAF Inhibitor Therapy. *Cancer Res.* **2019**, *79*, 2947–2961.

(48) Giuliano, M.; Shaikh, A.; Lo, H. C.; Arpino, G.; De Placido, S.; Zhang, X. H.; Cristofanilli, M.; Schiff, R.; Trivedi, M. V. Perspective on Circulating Tumor Cell Clusters: Why It Takes a Village to Metastasize. *Cancer Res.* **2018**, *78*, 845–852.

(49) Krause, L.; Herbst-Irmer, R.; Sheldrick, G. M.; Stalke, D. Comparison of Silver and Molybdenum Microfocus X-Ray Sources for Single-Crystal Structure Determination. *J. Appl. Crystallogr.* **2015**, *48*, 3–10.

(50) Sheldrick, G. M. SHELXT - Integrated Space-Group and Crystal-Structure Determination. *Acta Crystallogr. Sect. A Found. Crystallogr.* **2015**, *71*, 3–8.

(51) Sheldrick, G. M. Crystal Structure Refinement with SHELXL. *Acta Crystallogr. Sect. C Struct. Chem.* **2015**, *71*, 3–8.

Table of Contents graphic